DOUBLE LAYER EFFECTS ON
SHOCK WAVE PROPAGATION

THESIS

Shannon L. Walker, Captain, USAF
AFIT/GAP/ENP/99M-15

DEPARTMENT OF THE AIR FORCE
AIR UNIVERSITY
AIR FORCE INSTITUTE OF TECHNOLOGY

Wright-Patterson Air Force Base, Ohio

APPROVED FOR PUBLIC RELEASE; DISTRIBUTION UNLIMITED

Double Layer Effects

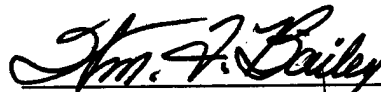on Shock Wave Propagation

THESIS
Shannon L. Walker
Captain

AFIT/GAP/ENP/99M-15
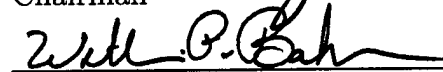
Double Layer Effects

on Shock Wave Propagation

Shannon L. Walker, B.S.

Captain

Approved:

Wm. F. Bailey   _5 Mar 99_
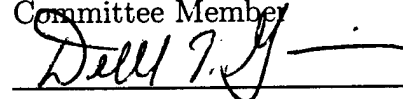
Dr. William F. Bailey   Date
Chairman

Will P. Baker   _5 Mar 99_

Dr. William P. Baker   Date
Committee Member

Derrill T. G   _8 Mar 99_

Maj Derrill T. Goldizen   Date
Committee Member

The views expressed in this thesis are those of the author and do not reflect the official policy or position of the Department of Defense or the United States Government.

AFIT/GAP/ENP/99M-15

Double Layer Effects

on Shock Wave Propagation

THESIS

Presented to the Faculty of the School of Engineering

of the Air Force Institute of Technology

Air University

In Partial Fulfillment of the

Requirements for the Degree of

Master of Science

Shannon L. Walker, B.S.

Captain

March 1999

Preface

Throughout the course of this work, I have become indebted to a number of individuals and institutions. I would first like to first thank God and the United States Air Force for the opportunity to study at AFIT. I would like to recognize my closest colleagues, Captains Chris Smithtro, Kelly Law, and Steve Novotny, and 1Lt Frank Tersigni, for their wit, wisdom, encouragement, and support with UNIX and Scientific Word. Two individuals around Wright-Patterson that have my gratitude are Erin Davis at the Major Shared Resource Center help desk and Pam McCarthy at the National Air Intelligence Center library, both for coming through in a pinch. I would also like to thank the staff at the AFIT library, especially Donna Gurnick for her enthusiasm and helpfulness. Much of this work could not be completed without the guidance of my advisor, Dr. William F. Bailey (AFIT/ENP); I am indebted for his insight, patience, direction, and encouragement. I would be greatly remiss if I did not recognize Major William Hilbun; his foray into the field made my research so much easier. Last, but definitely not the least, I must express my deepest appreciation to my wife and daughter for their faith, encouragement, and forbearance during this project. Daddy is done with his homework . . . for now.

Shannon L. Walker

Table of Contents

List of Figures

Abstract

An analysis and assessment of two mechanisms in plasma shock interactions was conducted under conditions typically encountered in a weakly ionized glow discharge. The mechanisms of a spatially-dependent electron temperature and additional electron impact ionization at the shock front were examined for effects on shock structure and propagation. These mechanisms were incorporated into an existing one-dimensional, time-dependent, fluid dynamics code that uses the Riemann problem as a basis and numerically solves the Euler equations for two fluids: the neutral gas and the charged component. The spatial variation in electron temperature was modeled as a shock-centered rise in temperature. Additional ionization was modeled by incorporating a variable electron temperature and a quasi-kinetic collision function, for both unrestricted ionization and ionization mitigated by ion-electron recombination. Introduction of a spatial variation in electron temperature resulted in a broadening and strengthening of the electric field associated with the electronic double layer (EDL) at the shock front. Results of unrestricted ionization were a broadening and strengthening of the electric field associated with the EDL, an acceleration of the neutral shock front, and the development of a neutral precursor ahead of the shock. Ion-electron recombination was seen to reduce these effects.

Double Layer Effects
on Shock Wave Propagation

I. Introduction

Interest in shock waves first appeared in aeronautics during World War II. At the time, supersonic flight was thought to be unobtainable due to aerodynamic and structural limitations. However, when dive-bombers entered steep dives, loss of aerodynamic control was attributed to the build up of shock waves on aircraft control surfaces as the flow over the wings became supersonic. This phenomenon spurred serious research efforts into the possibility of supersonic flight and soon after the war, the Bell X-1, piloted by Chuck Yeager, traversed the so-called sound barrier. This first step eventually led to such remarkable developments as the SR-71 and today's supersonic fighters.

A new dimension in supersonic aerodynamics may be emerging. Beginning in the early 1950s, Soviet researchers observed several phenomena associated with shock propagation in weakly ionized gases. Shocks have been seen to increase in velocity ((6), (28), (27), (12), (13), (15), (16)), yet disperse in thickness and reduce in strength ((26), (28), (30), (31)). Other structural modifications have been observed, such as an increase in shock stand off distance (29) and the appearance of a shock precursor–a region of elevated density, pressure, and temperature upstream from the shock front ((7), (11)). Also, the aerodynamic bodies in the flow experienced reduced aerodynamic drag and reduced heating of their surfaces ((29),(22:8)). Efforts to understand and capitalize on these effects have opened a new field of study–plasma aerodynamics.

Obviously, there are physical differences between ionized gases and unionized gases. Ionized gases are in a non-equilibrium state, with neutral, ion, and electron temperatures differing substantially. Ionized gases also interact strongly with electric and magnetic fields. At the shock front, electrons diffuse upstream due to their high mobility. In contrast, the ions, being less mobile, remain more strongly coupled to the neutral flow. As depicted in Figure 1, this charge separation results in an electronic double-layer (EDL) and an electric potential consistent with Poisson's equation,

$$-\nabla^2 \phi = \nabla \cdot \overline{E} = \frac{\zeta}{\epsilon_0} = \frac{e(n_i - n_e)}{\epsilon_0} \tag{1}$$

where ϕ is the electric potential, $\overline{E}$ is the electric field vector, ζ is the net charge density, e is the elementary charge, n_i and n_e are the ion and electron number densities, respectively, and ϵ_0 is the permittivity of free space. In one dimension, Poisson's equation reduces to

$$-\frac{\partial^2 \phi}{\partial x^2} = \frac{\partial E}{\partial x} = \frac{e(n_i - n_e)}{\epsilon_0} \tag{2}$$

The space charge electric field restricts the separation of ions and electrons. The potential drop, ϕ, is related to the electric field by the following:

$$\overline{E} = -\nabla \phi \tag{3}$$

1.1 Problem statement

This research effort used analytical and numerical techniques to characterize the double layer, which arises when a shock propagates in a weakly ionized gas, and assessed double layer influence on shock structure and propagation. The environment was limited to nonmagnetized, weakly ionized argon, for conditions typically encountered in a glow discharge: $P = 30\,\text{torr}$, $T = 300\,\text{K}$, $T_e = 2\,\text{eV}(= 23200\,\text{K})$, and
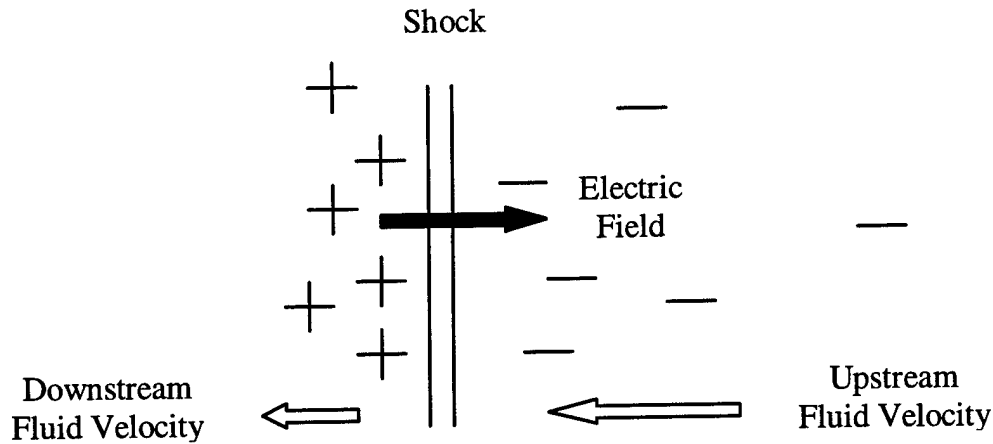
Figure 1   Electronic double layer at a stationary shock front in weakly ionized gas.

a fractional ionization of $\alpha = 10^{-6}$, where $\alpha = n_i/n_n$. Previous treatments simplify the problem by omitting several physical mechanisms. Some of these restrictions were lifted in order to investigate the contributions of these mechanisms upon shock structure and propagation. Analytical and numerical techniques were employed in a self-consistent solution of the resulting Euler equations. Specific attention was given to the contribution of the electric field generated by charge separation at the shock front. The self-consistent calculation of the field was also attempted in this research; the weakly ionized gas was represented as a set of three fluids coupled by collisions and the electric field. This would have employed analytical and numerical techniques in a self-consistent solution of the resulting Euler and Poisson equations. Details of this development can be found in Appendix B.

1.2   Importance of research

Being a relatively new field of study, the benefits of plasma aerodynamics have yet to be fully tapped. Hilbun (22:17) mentions several possible applications:

- Drag and heat transfer reduction of hypersonic vehicles: Several researchers have reported these effects ((8), (29)). Figure 2 depicts an advanced hypersonic vehicle concept that would employ the benefits of plasma aerodynamics (21).

3

AJAX Hypersonic Vehicle

Directed
Energy
Beam

Ionizer

MHD Generator

High Speed Propulsion

MHD Accelerator

Low Speed
Propulsion
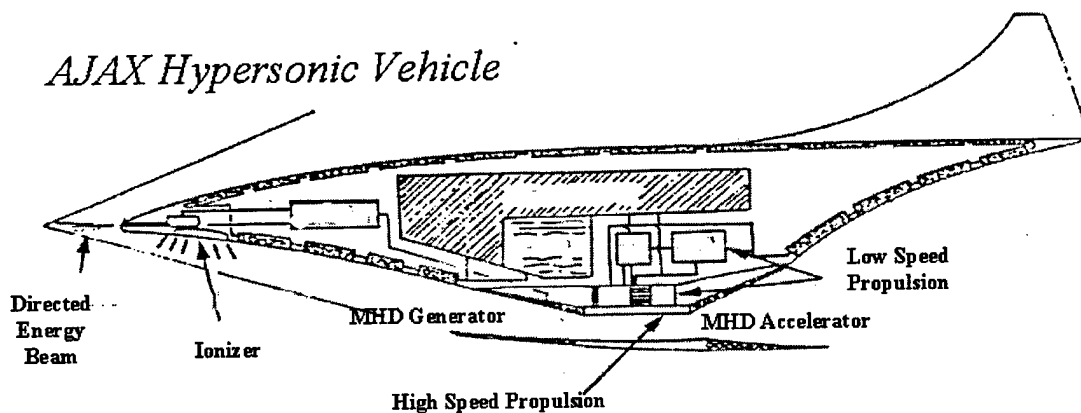
Figure 2 AJAX hypersonic vehicle concept (Ref: (21)).

- Aircraft without control surfaces: Control moments are generated by applying magnetic torques to the ionized fluid.

- Boundary-layer control: Laminar flow could be maintained for conditions in which turbulent flow or separation is expected by applying magnetic torques to the ionized flow.

- Reduction of radar cross section: For average flight conditions, radar signals, which are on the order of 10 GHz, could possibly be attenuated by maintaining a weakly ionized environment around an aircraft with fractional ionizations as low as 10^{-8}.

- Maintaining RF communication with spacecraft during reentry: Communications blackout is typically experienced due to high plasma frequencies around the spacecraft. The presence of a magnetic field yields different electromagnetic wave modes for a given frequency (37). Magnetic control of the reentry plasma could allow for non-attenuated wave modes.

1.3 Scope and limitations

The shocks investigated are one-dimensional, ideal processes. Shock phenomena are multi-dimensional problems; however, limiting the problems to one spatial

4

dimension allows normal shock relations to be used, which will be discussed in Chapter II. At the shock front, numerous viscous mechanisms occur. Since the research objective focuses on the motion of charged particles in the general area of the shock, these viscous effects are ignored. Therefore, the ideal equation of state can be used:

$$P = \rho \frac{k_B}{m} T \qquad (4)$$

where P is the pressure, ρ is the density, k_B is Boltzmann's constant, m is the molecular mass of the gas, and T is the temperature. The ideal assumption is valid since it has been experimentally determined that gases at low pressures (760 Torr or less) and high temperatures (273 K or more) behave in ideal fashion (4:15). Some researchers have suggested that perhaps weakly ionized gases behave in a non-ideal fashion ((32) and (35)). Saeks and Kunhardt (35) derive an equation of state that incorporates electrostatic pressure terms due to the plasma components. From this equation of state, an equation of the sound speed can be derived. Mishin (32) proposes a similar equation of state, yet his non-ideal terms are based on empirical calculations rather than a derivation employing Maxwell's equations.

Although much of the current research is conducted in glow discharge tubes, this research effort will focus on shock tube problems, also known as Riemann problems, as the instrument of investigation. A review of shock tube dynamics will occur in the next chapter. In a glow discharge tube, an electric field is applied to the gaseous medium, which causes electronic excitation (hence the glow) and ionization. Ion density is maintained via diffusional losses to the tube walls. In the shock tube, no initial electric field is present; however, it will be assumed that the fractional ionization is constant as well.

In addition to the presence of an ambient electric field, shock structure differs between those of shock tubes and discharge tubes. The shocks in discharge tubes are generated by a spark detonation–a momentary burst of energy. In shock tubes,

5

they are generated by a large pressure reservoir and are consistent with aerodynamic shocks; the drive of the aerodynamic vehicle provides the pressure reservoir similar to that of a shock tube. This begs the question as to whether different apparati of investigation yield different results. For a wide variety of gaseous media, Gorshkov, et al., (19) used a variety of plasmas to measure shock wave propagation–the plasmas of glow discharges, pulsed discharges, and decaying glow discharges–and found that "regardless of the kind of gas and the type of discharge, the behavior of the electron component in the region of the shock wave front had the same characteristic features". In addition, similar results were obtained by researchers ((8), (29)) while conducting tests in a completely different experimental setup–aerodynamic bodies moving through a weakly ionized media.

In real gases, there is a plethora of energy sinks to consider in simulated hydrodynamic phenomena. Some of these sinks are molecular, such as rotation, vibration, and dissociation. Other sinks are both molecular and atomic, such as electronic excitation and ionization. In the case of the present research, the molecular energy sinks were eliminated from consideration by studying a monatomic gas: argon. To further simplify the problem, electronic excitation was ignored–argon atoms are either ionized or not, and energy gained is transferred to either ionization or kinetic energy.

1.4 Research Approach

Chapter II briefly covers the background material of plasma aerodynamics. Before the effects of plasma can be studied, a brief review of the basics of one-dimensional, compressible fluid dynamics in the absence of plasma is provided. Shock tubes are also afforded a brief description. Then, the phenomena associated with shock wave propagation in weakly ionized gases are identified and described. Finally, possible physical mechanisms behind these phenomena are identified: vi-

brational relaxation, thermal inhomogeneities, ion-acoustic wave damping, and additional ionization at the shock front.

Some of the previous analytical treatments of shock propagation in weakly ionized gases are illustrated in Chapter III. The works of Avramenko, et al., (5) and Hilbun (22) serve as the main fare. As with any analytic treatment of complex physical phenomena, these works incorporate a number of restrictions that may preclude an accurate evaluation of the electric field and its affect on shock structure and propagation. These restrictions are:

- Two-fluid approximation. The charged components of the plasma are combined into one fluid by assuming that the electron momentum is steady-state for laboratory conditions. This restriction prevents ions and electrons from moving independently of each other, which is necessary in order to fully characterize the double layer influence on shock structure and propagation in weakly ionized gases.

- Approximation of electric field. This is a by-product of the two-fluid approximation. With steady-state electrons, the electric field balances the pressure gradient force and momentum coupling, which allows the electric field to be approximated by means of the electron pressure gradient, as opposed to Poisson's equation (Equation 2).

- Constant electron temperature. This is assumed to be the case in glow discharges due to the extremely short relaxation time of the electrons, meaning any energy gained is quickly lost.

- Static neutral profiles. In the work of Avramenko, the physical properties of the neutrals near the shock front are specified, which prevents the charged components from affecting the neutrals.

- Constant fractional ionization. There are no production or loss terms; the plasma cannot decay nor can additional ionization occur at the shock front.

7

- Ideal behavior. Electrostatic pressures are prevented from affecting the gas pressure.

Two of these restrictions are lifted in Chapter IV. Research indicates that electrons undergo heating at the neutral shock front as they pass through the EDL; therefore, variable electron temperature at the shock front is investigated. Electron energies for equilibrium laboratory conditions are generally lower than the ionization potentials of the gaseous media studied. Research indicates, however, that additional ionization may occur at the shock front; therefore, additional ionization is investigated, as well. For both cases, the numerical results from modifications to Hilbun's plasma code are examined for effects on the EDL, shock structure, and shock propagation. This research effort also attempted to lift the two-fluid approximation; however, the difference in computational time step for electron motion compared to heavy particle motion proved to be prohibitively small to be accomplished within the time and computational limitations imposed upon the present research. The development of this attempt can be found in Appendix B.

1.5 Product of research

This research has produced a modification to Hilbun's one-dimensional plasma code (22:27) that makes allowances for variable electron temperature and additional ionization at the shock front. The aforementioned restrictions–constant electron temperature and constant fractional ionization–are lifted. Numerical data from this code modification can provide a non-restricted data set to compare to the restricted analytical and numerical solutions of Avramenko and Hilbun. This comparison can illuminate any significant contributions to shock structure and propagation from the double layer electric field as enhanced by variable electron temperature and additional ionization over a range of discharge parameters common to plasma aerodynamics.

8

II. Background

2.1 Compressible flow in neutral gas

Compressible flow is that branch of fluid dynamics that concerns itself with fluid media in which the density can no longer be considered constant. An important phenomena that occurs due to compressibility is the shock wave. A full treatment of the shock wave dynamics is beyond the scope of the present research. However, Hilbun stated it very simply: "Shock formation can be understood by considering the nonlinear terms in the fluid equations. These nonlinear terms cause portions of the wave with a larger amplitude to travel at a higher velocity than portions of the wave with a smaller amplitude. Thus the wave front steepens until it becomes multivalued and 'breaks' (22:4)". The width of a typical shock front for aerodynamic conditions is on the order of 10^{-4} cm, or several mean free paths.

2.1.1 One dimensional flow.
Shock waves in any environment are three dimensional structures. Although, in some cases, it is feasible to model them in one dimension. One such case would be at the nose of a supersonic aircraft. When the shock is modeled in one dimension, the shock is normal to the free stream and is called a normal shock. Motion in wind tunnels, shock tubes, and gas discharge tubes generally assume constant area flow and the normal shock relations outlined below can be applied to them.

Most compressible fluid texts provide a development of normal shock relations. A brief review is warranted here with the help of Anderson (4). In order to investigate any fluid flow process, it is necessary to begin with the continuity, momentum, and energy equations. In the analysis of normal shocks, the flow is assumed to be steady and inviscid, meaning that there are no losses due to friction, diffusion, and

9

thermal conduction. The continuity equation is then

$$\frac{\partial}{\partial t}\rho + u\frac{\partial}{\partial x}\rho = 0$$

$$\rho_1 u_1 = \rho_2 u_2 \tag{5}$$

where ρ is the fluid density, u is the free stream fluid velocity, and the subscripts 1 and 2 represent conditions upstream and downstream from the shock, respectively. This simply states that the mass flux on either side of the shock is constant. As in the case with normal shocks, when $u_1 > u_2$, then $\rho_2 > \rho_1$. The momentum equation is given by

$$\frac{\partial}{\partial t}(\rho u) + u\frac{\partial}{\partial x}(\rho u) + \frac{\partial}{\partial x}P = 0$$

$$P_1 + \rho_1 u_1^2 = P_2 + \rho_2 u_2^2 \tag{6}$$

where P is the fluid pressure. The quantity ρu^2 is often referred to as the dynamic pressure. The energy equation is given by

$$\frac{\partial}{\partial t}(\rho u^2) + u\frac{\partial}{\partial x}(\rho u^2) + \frac{\partial}{\partial x}w = 0$$

$$\frac{u_1^2}{2} + \frac{P_1}{\rho_1} + w_1 + Q = \frac{u_2^2}{2} + \frac{P_2}{\rho_2} + w_2 \tag{7}$$

where Q is the heat addition and w is the thermal energy, given by

$$w = c_V T = \frac{1}{\gamma - 1}\frac{k_B T}{m} \tag{8}$$

where γ is the ratio of specific heat at constant volume to the specific heat at constant pressure, c_V/c_P, which is never more than 5/3. Incorporating the definition of the thermal energy and the equation of state, Equation 4, the energy equation becomes

$$\frac{u_1^2}{2} + \frac{\gamma}{\gamma - 1}\frac{k_B T}{m} + Q = \frac{u_2^2}{2} + \frac{\gamma}{\gamma - 1}\frac{k_B T}{m} \tag{9}$$

10

The speed of sound is an important parameter in the analysis of compressible flow. Sound waves impart small deviations in the fluid parameters; therefore, the propagation of a sound wave is an isentropic process. A perturbation analysis of Equations 5 and 6 yields the following isentropic relationship for the speed of sound:

$$a = \sqrt{(\frac{\partial P}{\partial \rho})_s} \tag{10}$$

where s indicates an isentropic process. Applying the ideal equation of state, Equation 4, and the following isentropic relation,

$$\frac{P_2}{P_1} = (\frac{\rho_2}{\rho_1})^\gamma \tag{11}$$

Equation 10 becomes

$$a = \sqrt{\gamma \frac{k_B T}{m}} \tag{12}$$

Note that the sound speed, depending on the value of γ, is about two-thirds to three-quarters of the average molecular velocity from kinetic theory, $v_{ave} = \sqrt{8 k_B T / \pi m}$.

Another important parameter related to the sound speed is the Mach number:

$$M = u/a \tag{13}$$

The Mach number is also a measure of the directed energy of the fluid flow compared to the random molecular motion, as shown by the following ratio of the directed energy to the thermal energy:

$$\frac{u^2/2}{w} = \frac{u^2/2}{c_V T} = \frac{u^2/2}{\frac{1}{\gamma-1}\frac{k_B T}{m}} = \frac{\gamma u^2/2}{a^2/(\gamma-1)} = \frac{\gamma(\gamma-1)}{2} M^2 \tag{14}$$

11

Obviously, $M = 0$ means that there is no directed energy, as M approaches ∞, almost all the fluid's energy is directed, and $M = 1$ means that the flow velocity exceeds the thermal velocity by a factor of $\sqrt{\gamma}$.

From these simple relationships come the normal shock relations, which define flow variable ratios across the shock front. For supersonic flow, the Prandtl relation states that $M_1 > 1$ and $M_2 < 1$. From the Prandtl relation and the energy equation, the post-shock Mach number is given by

$$M_2^2 = \frac{1 + \frac{\gamma-1}{2}M_1^2}{\gamma M_1^2 - \frac{\gamma-1}{2}} \tag{15}$$

The following ratios can also be derived from the energy equation:

$$\frac{P_2}{P_1} = 1 + \frac{2\gamma}{\gamma+1}(M_1^2 - 1) \tag{16}$$

$$\frac{\rho_2}{\rho_1} = \frac{u_1}{u_2} = \frac{(\gamma+1)M_1^2}{2 + (\gamma-1)M_1^2} \tag{17}$$

$$\frac{T_2}{T_1} = \frac{P_2}{P_1}\frac{\rho_1}{\rho_2} \tag{18}$$

Note that all post-shock flow variables can be determined by the upstream flow variables and Mach number.

2.1.2 Shock tube relations. An important instrument for studying normal shocks is the shock tube. The shock tube is a tube of constant cross sectional area closed at both ends, with a high pressure reservoir (Region 4) separated from a low pressure region (Region 1) by a diaphragm, as illustrated in Figure 3. Regions 4 and 1 are also referred to as the driver section and the driven section, respectively. The gases in these regions can also have different temperatures and molecular masses.

When the diaphragm is broken, a shock propagates into Region 1 with speed c, and expansion waves propagate into Region 4, lowering P_4 to P_3, as shown in Figure 4. As the shock plows into Region 1, it increases the pressure from P_1 to P_2, and induces mass motion, u, in Region 2. The interface between the driver and driven section is called the contact discontinuity, which also propagates with velocity u. The flow field in the shock tube after the diaphragm is broken is completely determined by the initial conditions in Regions 1 and 4. The following equation relates the initial, quiescent conditions to the dynamic conditions:

$$\frac{P_4}{P_1} = \frac{P_2}{P_1}(1 - \frac{(\gamma_4 - 1)\frac{a_1}{a_4}(\frac{P_2}{P_1} - 1)}{\sqrt{2\gamma_1(2\gamma_1 + (\gamma_1 + 1)(\frac{P_2}{P_1} - 1))}})^{-2\gamma_4/(\gamma_4 - 1)} \qquad (19)$$

which gives the pressure ratio across the shock front, P_2/P_1, as an implicit function of the initial pressure ratio across the shock tube diaphragm, P_4/P_1. After a period of time has passed since the initial onset of the shock, the shock propagation in the Riemann problem becomes relatively constant; therefore, the normal shock relations can be used and the resulting Mach number is easily determined from Equation 16. In spite of the interesting effects that occur in the shock tube, the present research focuses only on the shock.

2.2 Observations in Weakly Ionized Gases

When shocks propagate in weakly ionized gases, a number of phenomena have been observed that deviate from what is observed in neutral gas flows. Four of these phenomena are investigated in this work:

- Shock waves in plasma have an anomalously high propagation velocity. In some cases when the shock entered the plasma, the shock velocities nearly doubled ((6), (28), (27), (12), (13), (15), (16)).

Driver section   Driven section

| 4 | 1 |

Diaphragm

P_4

P_1

Pressure

Distance
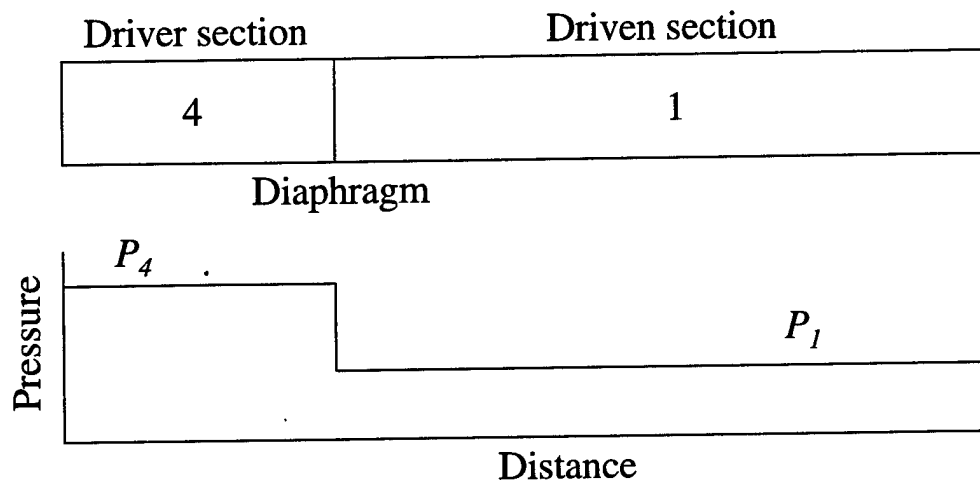
Figure 3   Initial shock tube conditions (Ref: (4)).

Expansion   Contact
waves   discontinuity   Shock

| 4 | | 3 | u | 2 | c | 1 |

P_4

$P_3 = P_2$

P_1

Pressure

Distance
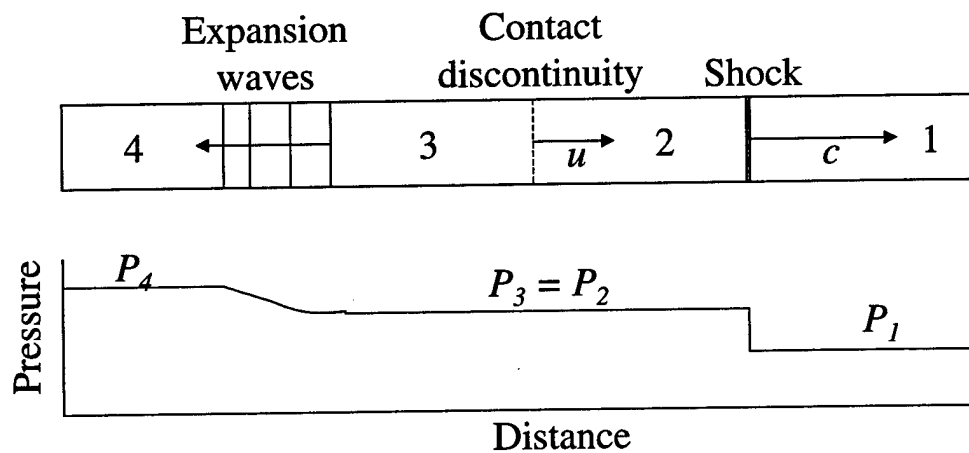
Figure 4   Shock tube dynamics. The shock moves into the quiescent gas in Region
1 at speed c. The contact discontinuity moves with the fluid behind the
shock at speed u. The expansion waves propagate into Region 4 (Ref:
(4)).

14

- Significant broadening and dispersion of the shock front occurs in weakly ionized gases. The steep gradients in the fluid flow variables that define the shock are significantly reduced ((26), (30)).

- A precursor exists ahead of the shock wave. Precursors are regions of elevated pressure that precede the shock by millimeters or centimeters ((7), (19), (11)).

- Shock strength is reduced. In some cases the cross shock pressure ratio was cut in half ((28), (31)).

In addition to these basic aspects of shock modification in a weakly ionized gas, there are three phenomena that are not examined due to the nature of the model used in this research:

- Modification of aerodynamic drag ((8), (18)).

- Reduced heat flux to aerodynamic surfaces (22:8).

- Increase in shock stand-off distance (29).

The possible physical mechanisms behind these observed phenomena are described below. They are post-shock vibrational relaxation, thermal inhomogeneities in the plasma, and ion-acoustic wave damping. As a shock propagates into a region of the gas that is vibrationally excited, the gas gives up vibrational energy to the flow, which accelerates the shock. Post-shock vibrational relaxation is obviously not a contributor to the observed phenomena in monatomic gases, such as argon.

2.2.1 Thermal inhomogeneities. The phenomena mentioned above are also observed in monatomic gases. Researchers have suggested that thermal inhomogeneities in the weakly ionized gas to be the chief cause of the effects ((2), (14)). Elevated temperatures can be the by-product of plasma generation or decay. It is known that shocks move faster in media with higher temperatures, as illustrated in Figure 5, where T_1 and V_1 represent the initial gas temperature and shock velocity,
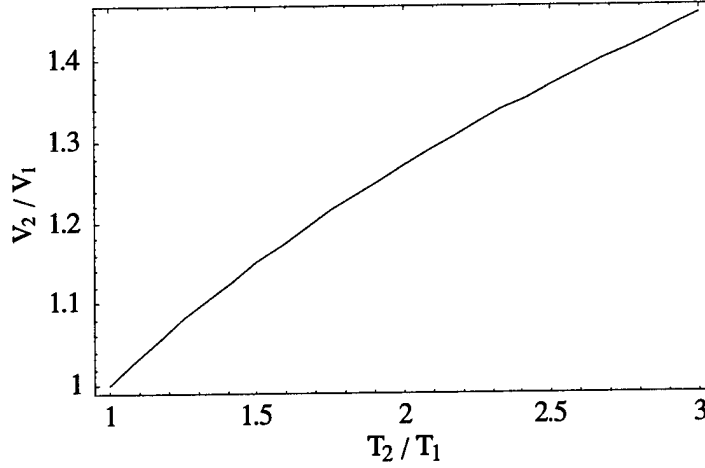
Figure 5   Acceleration of a Mach 2 shock as a function of thermal inhomogeneity (Ref: (22)).

respectively, and T_2 and V_2 represent the gas temperature and shock velocity, respectively, in a region where $T_2 > T_1$. The increase in shock velocity is primarily due to the fact that the sound speed increases as temperature increases (Equation 12). The shock accelerates because it encounters an area in which the gas molecules are of higher energy; therefore, less energy from the shock is needed to accelerate the upstream molecules and the shock wave accelerates. Hilbun devoted a large portion of his research to thermal inhomogeneities and developed a two-dimensional, time-dependent thermal code to investigate this mechanism (22:28). The thermal cause has its detractors though ((26), (28), (6), (27)), who have shown that shock velocities in plasma exceed those that would be expected from a solely thermal configuration.

2.2.2   Ion-acoustic wave damping.

According to Jones (24:77), ion-acoustic waves are purely electrostatic waves in an nonmagnetized, ion-electron plasma. The dispersion relation for such waves is given by

$$1 - \frac{\omega_e^2}{\omega^2 - k^2 v_e^2} - \frac{\omega_i^2}{\omega^2 - k^2 v_i^2} = 0 \tag{20}$$

16

where ω and k are the frequency and wave number of the disturbance, respectively, ω_e and ω_i are the electron and ion plasma frequencies, respectively, and v_e and v_i are the electron and ion thermal velocities, respectively. It is assumed that $\omega \ll \omega_e$ and that $T_e \gg T_i$, which leads to $v_i \ll \omega/k \ll v_e$, so that the dispersion relation reduces to

$$1 + \frac{\omega_e^2}{k^2 v_e^2} - \frac{\omega_i^2}{\omega^2 - k^2 v_i^2} = 0 \tag{21}$$

If it is also assumed that $\omega \ll \omega_i$, and after some algebraic manipulation, the group velocity can be extracted from the dispersion relation:

$$\left(\frac{\omega}{k}\right)^2 = v_i^2 + v_e^2 \left(\frac{\omega_i}{\omega_e}\right)^2 \tag{22}$$

The plasma frequency is given by $\omega_p^2 = n_p q^2 / \epsilon_0 m_p$, where n_p is the particle number density, and q is the charge on the particle. After applying Equation 12 to both v_e and v_i, and if it is also assumed that the plasma is quasi-neutral and singly ionized, then the ion-acoustic velocity is given by

$$\frac{\omega}{k} = v_{ia} = \sqrt{\frac{k_B}{m}(\gamma_i T_i + \gamma_e T_e)} \simeq \sqrt{\frac{k_B T_e}{m}} \tag{23}$$

where γ_e is taken to be unity. According to Jones (24:78), the ion-acoustic wave is a compression wave in a plasma analogous to an ordinary sound wave in air, where the ions provide most of the inertia of the wave, while the electrons provide the pressure to drive the wave. Note, however, that v_{ia} can be an order of magnitude larger than a, depending upon the ratio T_e/T_i.

Several researchers ((26), (6), (7), (28)) have suggested that it is the damping of these waves that accelerate shocks in plasma. Mishin (28) stated it most eloquently: "The high effective sound velocity in the plasma–several times the thermal sound velocity–can be explained by assuming that an intense mechanism is operating to

17

convert some of the energy of the shock wave into kinetic energy of the neutral particles ahead of the shock front." In the thermal case, the shock accelerates because it encounters an area in which the molecules are of a higher energy; therefore, less energy from the shock is needed to move the molecules and the shock accelerates. In the case of plasmas, the electric field with ion-neutral momentum coupling serves to energize the particles ahead of the shock, and the shock does not expend as much energy to move through the gas. Basargin and Mishin (6) state that the shock propagation velocity is a hybrid of the non-plasma shock velocity and the ion-acoustic wave velocity.

2.2.3 Additional ionization. Some researchers indicate that additional ionization may contribute to the observed plasma effects (19). As electrons are accelerated by the space charge field, a small fraction of them reach kinetic energies on par with the first ionization potential of the gas. The charged particles produced at the shock front are generally restricted to that location due to the local fluid dynamics, the electric field, and the mutual attraction of the charged particles. The net effect of this ionization is an exponential increase in charged particles with time, which increases the local fractional ionization at the shock front, making ion-acoustic wave damping more effective. This mechanism is explored in depth in Chapter IV.

III. Literature Review

The effects of plasma on shock wave propagation have been studied since the 1950s. In 1965, Jaffrin (23:616) attempted to numerically solve the Navier-Stokes equations for a ternary fluid of neutrals, ions, and electrons. Due to the complexity of the equations and the limited computational resources at that time, all three fluids were combined into one in order to facilitate a solution. His solution for weakly ionized gases yielded a charged precursor upstream from the shock, but the neutral flow was unaffected. The analytical foundation of shock wave structure in weakly ionized gases was developed in the early 1980s by Avramenko, Rukhadze, and Teselkin (5) and is therefore reviewed in detail. Hilbun extended their steady-state approach (22:69) and continued with a three-pronged, time-dependent approach, examining plasma effects, post-shock vibrational relaxation, and thermal inhomogeneities. The present research is an extension of Hilbun's investigation of plasma effects.

3.1 Steady State Treatment

3.1.1 Analytical. Avramenko, et al., (5) sought an analytical solution to the problem of shock propagation in weakly ionized gases, particularly focusing on the flow variables of the charged components thereof. In order to accomplish this feat, they applied all of the restrictions described in Section 1.4. These restrictions were the two-fluid approximation, the electron pressure gradient approximation of the electric field, constant electron temperature, static neutral profiles, and no production or loss terms. The treatment further imposes the following restrictions:

- The ion temperature is constant through the shock.

- The problem is restricted to one spatial dimension.

- Charge neutrality is maintained.

19

- The neutral density and velocity profiles are prescribed by a step function. In front of the shock the fluid is static, while behind the shock the neutral velocity is given by u.

The complete, nonmagnetized ion and electron momentum equations are given below, where V is the fluid velocity, ν is the collision frequency, and the subscripts, n, i, and e represent neutrals, ions, and electrons, respectively.

$$\frac{\partial}{\partial t}(\rho_i V_i) + V_i \frac{\partial}{\partial x}(\rho_i V_i) = -\nabla P_i + \frac{\rho_i e E}{m} - \rho_i \nu_{ie}(V_i - V_e) - \rho_i \nu_{in}(V_i - V_n) \quad (24)$$

$$\frac{\partial}{\partial t}(\rho_e V_e) + V_e \frac{\partial}{\partial x}(\rho_e V_e) = -\nabla P_e - \frac{\rho_e e E}{m_e} - \rho_e \nu_{ei}(V_e - V_i) - \rho_e \nu_{en}(V_e - V_n) \quad (25)$$

After applying the above constraints, the electron momentum equation reduces to

$$-\frac{k_B}{m_e}\frac{\partial(\rho_e T_e)}{\partial x} - \frac{\rho_e e E}{m_e} - \rho_e \nu_{en}(V_i - V_n) = 0 \quad (26)$$

and the electric field can be approximated as

$$E \approx -\frac{k_B}{\rho_e e}\frac{\partial(\rho_e T_e)}{\partial x} - \frac{m_e \nu_{en}}{e}(V_i - V_n) \quad (27)$$

The two-fluid approximation is completed after substituting the electric field into Equation 24, and assuming quasi-neutrality, in which $n_e \simeq n_i$:

$$\frac{\partial}{\partial t}(\rho_i V_i) + V_i \frac{\partial}{\partial x}(\rho_i V_i) = -\frac{\partial P_i}{\partial x} - \frac{k_B}{m}\frac{\partial(\rho_i T_e)}{\partial x} - \left(\frac{m_e}{m}\frac{\nu_{en}}{\nu_{in}} + 1\right)\rho_i \nu_{in}(V_i - V_n) \quad (28)$$

20

The collision frequency is given by Gombosi (17:99) as

$$\nu_{12} = 2\sigma_{12}n_2\sqrt{\frac{2k_B}{\pi}\left(\frac{T_1}{m_1} + \frac{T_2}{m_2}\right)} \tag{29}$$

where the subscript 1 represents the particle that collides, subscript 2 represents the particle that is impacted, and σ is the collision cross section. When applying Equation 29 to ion momentum equation, the mass and collision frequency ratio term is much less than unity and, therefore, neglected. Next, the one-dimensional ion pressure gradient is isothermally expanded using the ideal gas law (Equation 4). Then, the ion temperature is dropped since $T_e \gg T_i$, the convection derivative is expanded, and the non-steady term is dropped. Finally, recall the ion-acoustic velocity, Equation 23, and the charged component momentum becomes:

$$\rho_i\left(\frac{\partial V_i}{\partial t} + V_i\frac{\partial V_i}{\partial x}\right) = -(v_{ia}^2 + V_i^2)\frac{\partial \rho_i}{\partial x} - \rho_i\nu_{in}(V_i - V_n) \tag{30}$$

The hydrodynamic fluid velocity, V, is never greater than c, the shock velocity; therefore $V \leq Ma$. The ratio V_i^2/v_{ia}^2 is approximately $\gamma M^2 T_i/T_e$. Since electron temperatures are usually two orders of magnitude greater than ion temperatures, and if the Mach number remains near unity, the ratio is much less than unity and the ion velocity is neglected. Therefore, Equation 30 becomes

$$\frac{\partial V_i}{\partial t} + V_i\frac{\partial V_i}{\partial x} = -\frac{v_{ia}^2}{\rho_i}\frac{\partial \rho_i}{\partial x} - \nu_{in}(V_i - V_n) \tag{31}$$

Since Avramenko uses a prescribed solution for the neutral velocity and if the upstream ion-neutral collision frequency, ν_{in}, can be treated as a parameter, then there are two unknowns, V_i and ρ_i. The continuity equations for the neutral and charged components round out the required number of equations to solve the

21

problem:

$$\frac{\partial \rho_i}{\partial t} + \frac{\partial}{\partial x}(\rho_i V_i) = 0 \qquad (32)$$

$$\frac{\partial \rho_n}{\partial t} + \frac{\partial}{\partial x}(\rho_n V_n) = 0 \qquad (33)$$

Even though Equation 33 is a third equation, it will be used to establish boundary conditions.

The equations are solved in the shock-fixed frame; therefore, it is necessary to introduce the transformation equations. The independent variable in this frame is $\xi = x - ct$, where c is the shock velocity in the "laboratory" frame. In the shock frame, the shock remains fixed at $\xi = 0$, while the upstream fluid is moving at $V = -c$. The differential transformations are:

$$\frac{\partial}{\partial t} = \frac{\partial}{\partial \xi}\frac{\partial \xi}{\partial t} = -c\frac{\partial}{\partial \xi}, \qquad \frac{\partial}{\partial x} = \frac{\partial}{\partial \xi}\frac{\partial \xi}{\partial x} = \frac{\partial}{\partial \xi} \qquad (34)$$

The velocity transformations are:

$$V_i \rightarrow y_i = c - V_i, \qquad V_n \rightarrow y_n = c - V_n \qquad (35)$$

where y_n and y_i are the neutral and ion velocities in the shock frame, respectively.

Now both ion and neutral continuity equations and the momentum equation can be transformed. Since ξ incorporates both variables x and t, the partial derivatives are also transformed into total derivatives.

$$-c\frac{d\rho_i}{d\xi} + \frac{d}{d\xi}(\rho_i(c - y_i)) = 0$$
$$\frac{\rho_i}{\rho_{i0}} = \frac{y_{i0}}{y_i} = \frac{c}{c - V_i} \qquad (36)$$

22

Here, ρ_{i0} is the undisturbed upstream ion density and the ion velocity far upstream of the shock, V_{i0}, is assumed to be zero. The neutral continuity equation transforms similarly, with the exception that neutral velocity and density profiles are prescribed by step functions at the shock.

$$
\begin{aligned}
-c\frac{d\rho_n}{d\xi} + \frac{d}{d\xi}(\rho_n(c - y_n)) &= 0 \\
\frac{\rho_{n1}}{\rho_{n0}} &= \frac{y_{n0}}{y_{n1}} = \frac{c}{c - u}
\end{aligned}
\tag{37}
$$

Here, ρ_{n1}/ρ_{n0} is the neutral density ratio across the shock and u is constant neutral velocity behind the shock. Equation 31 becomes

$$
\begin{aligned}
-c\frac{d(c - y_i)}{d\xi} + (c - y_i)\frac{d(c - y_i)}{d\xi} &= -\frac{v_{ia}^2}{\rho_i}\frac{d\rho_i}{d\xi} - \nu_{in}((c - y_i) - (c - y_n)) \\
\frac{d}{d\xi}(\frac{y_i^2}{2}) + \frac{v_{ia}^2}{\rho_i}\frac{d\rho_i}{d\xi} - \nu_{in}(y_i - y_n) &= 0
\end{aligned}
\tag{38}
$$

The shock-frame portion of Equation 36 is now inserted into the ion momentum equation:

$$
\frac{d}{d\xi}(\frac{y_i^2}{2} - v_{ia}^2 \ln(\frac{y_i}{c})) - \nu_{in}(y_i - y_n) = 0
\tag{39}
$$

Due to the neutral step functions, this differential equation must be solved in two parts: for the post-shock region, $\xi < 0$, and the upstream region, $\xi > 0$, with continuity of both V_i and ρ_i maintained at $\xi = 0$. The post-shock region is solved first. The key to the solution is the assumption that there are no forces acting on the fluid behind the shock; therefore, $dV_i/d\xi = 0$. In the laboratory frame, the neutral velocity is a constant value of u in this region; therefore, $y_i = c - V_i$ and $y_n = c - u$. After introducing these relations, expressing the ratio V_i/c as $\hat{V}$, and simplifying under the assumption that $V_i^2/v_{ia}^2 \ll 1$, Equation 39 can be rearranged

23

as such:

$$\frac{d\hat{V}}{d\xi} = \frac{c\nu_{in}}{v_{ia}^2}(\frac{u}{c} - \hat{V})(1 - \hat{V}) = 0 \tag{40}$$

The two possible solutions are $\hat{V} = 1$ or $\hat{V} = u/c$. The first solution means that $V_i = c$; this is only possible for shocks moving into a vacuum, where $\rho_{n0} = 0$. Since a general solution is sought, then $\hat{V} = u/c$ and $V_i = u$. Applying the neutral continuity equation, Equation 37, yields the following solution:

$$V_i = u = c(1 - \frac{\rho_{n0}}{\rho_{n1}}) \tag{41}$$

for the post-shock ion velocity in the laboratory frame. Equation 36 provides the post-shock ion density:

$$\rho_i = \rho_{i0}\frac{c}{c - V_i} = \rho_{i0}\frac{c}{c - u} = \rho_{i0}\frac{\rho_{n1}}{\rho_{n0}} \tag{42}$$

It is now possible to obtain the solution upstream from the shock. In the laboratory frame, the neutral velocity is assumed to be zero in this region; therefore, $y_i = c - V_i$ and $y_n = c$. After substituting these, $\hat{V} = V_i/c$, and applying the assumption $V_i^2/v_{ia}^2 \ll 1$, Equation 39 becomes

$$\frac{1}{\hat{V}(1 - \hat{V})}\frac{d\hat{V}}{d\xi} = \frac{c\nu_{in}}{v_{ia}^2} \tag{43}$$

Integrating from $\xi = 0$ where, from continuity with the post-shock region, $\hat{V} = u/c$, to some positive ξ and $\hat{V}$, yields the following,

$$\int_{u/c}^{\hat{V}} \frac{d\hat{V}}{\hat{V}(1 - \hat{V})} = \int_0^\xi \frac{c\nu_{in}}{v_{ia}^2}d\xi$$

$$\hat{V} = \frac{1}{1 + (\frac{c}{u} - 1)\exp(\frac{c\nu_{in}}{v_{ia}^2}\xi)} = \frac{1}{1 + (\frac{1}{\frac{\rho_{n1}}{\rho_{n0}}-1})\exp(\frac{c\nu_{in}}{v_{ia}^2}\xi)} \tag{44}$$

24

Avramenko introduced the following quantities to simplify the solution:

$$\mu = \ln(\frac{\rho_{n1}}{\rho_{n0}} - 1), \qquad \xi_0 = \frac{V_{ia}^2}{c\nu_{in}^{(0)}} \qquad (45)$$

where ξ_0 is the characteristic width of the precursor and $\nu_{in}^{(0)}$ is taken to be ambient upstream ion-neutral collision frequency, given by Equation 29. The solution of the upstream ion velocity in the laboratory frame is

$$V_i = \frac{c}{1 + \exp(\frac{\xi}{\xi_0} - \mu)} \qquad (46)$$

Calling upon Equation 36, the upstream ion density is given by:

$$\rho_i = \rho_{i0} \frac{c}{c - V_i} = \rho_{i0}(1 + \exp(\mu - \frac{\xi}{\xi_0})) \qquad (47)$$

Now, examine the solution for a shock where $M = 2$ for argon, where $\gamma = 5/3$ and $\alpha = 10^{-6}$. Equation 17 yields the following neutral ratios: $\rho_2/\rho_1 = 2.285$ and $u_2/u_1 = 0.438$. The ambient upstream conditions[1] of $T_{i,n} = 300\,\mathrm{K}$, $T_e = 2\,\mathrm{eV}(= 23200\,\mathrm{K})$, $P_{n0} = 30\,\mathrm{torr}$, and $\sigma_{in} = 4 \times 10^{-21}\,\mathrm{m}^2$, yield a sound speed of $c = 323\,\mathrm{m/s}$, a shock speed of $c = 645\,\mathrm{m/s}$, and a precursor width of $\xi_0 = 3.4\,\mathrm{mm}$. The solution of the charged component velocity is shown in Figure 6, and the density is shown in Figure 7.

Recall Equation 27, the electric field approximation. Hilbun has shown that the collision term is negligible (22:75) and the field approximation is easily converted to:

$$E \approx -\frac{k_B}{e\rho_i} \frac{d(\rho_i T_e)}{d\xi} \qquad (48)$$

---

[1]Unless otherwise indicated, these values will serve as the ambient upstream conditions for the remainder of the present research.
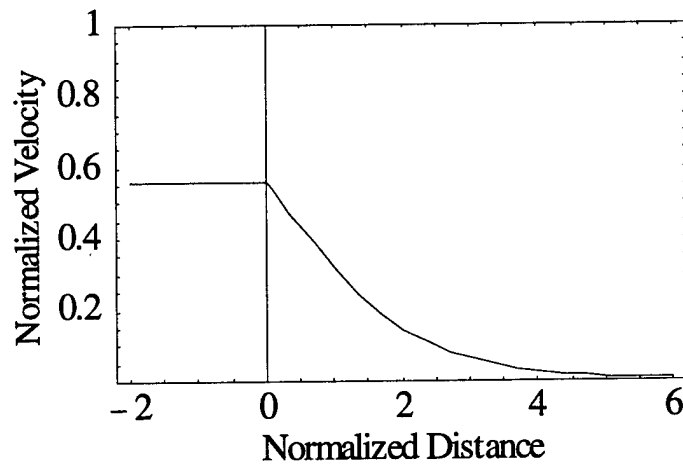
Figure 6   Steady state analytical solution of charged component velocity for a Mach 2 shock in argon.   Velocity is normalized to the shock velocity, c.   Distance is normalized by $\xi_0 = 3.4\,\text{mm}$.
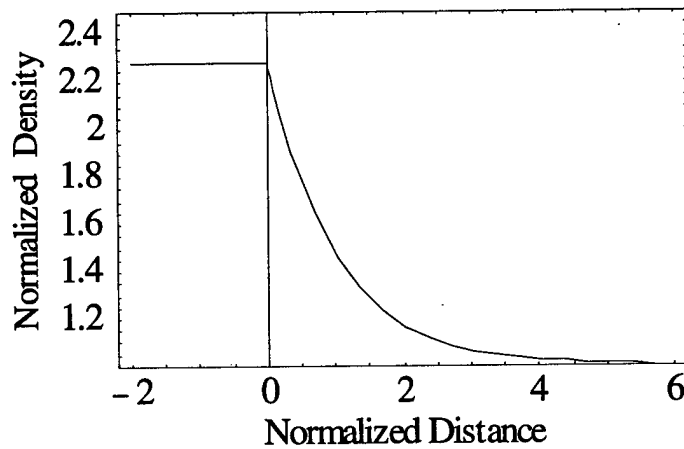
Figure 7   Steady state analytical solution of charged component density for a Mach 2 shock in argon.   Density is normalized to the upstream charged component density.   Distance is normalized by $\xi_0 = 3.4\,\text{mm}$.

Figure 8   Steady state analytical approximation of the electric field in the vicinity of a Mach 2 shock in argon.   Distance is normalized by $\xi_0 = 3.4\,\mathrm{mm}$.

In the post-shock region, the field approximation is zero since ρ_i is constant.   In the far upstream regions the field is zero because $\rho_i = \rho_{i0}$.   Just ahead of the shock, the electric field becomes

$$E \approx \frac{k_B T_e}{e\xi_0}(1 - \frac{\rho_{i0}}{\rho_i}) = \frac{k_B T_e}{e\xi_0}\frac{V_i}{c} \qquad (49)$$

Recalling Equation 36, the electric field approximation has the same functional form as the charged component velocity in the upstream region, as shown in Figure 8. Although, in reality, since the electric field drives the charged particles, the charged component velocity follows the form of the electric field.   The potential drop, as determined by Equation 3, experienced by a charged particle in this electric field is about $-1.5\,\mathrm{V}$.

3.1.2   Steady State Numerical Analysis .   Hilbun (22:69) initially obtained estimates of the flow field variables and electric field by an extension of Avramenko's steady-state approach.   He refined the neutral velocity and density profiles at the

shock front with a more physical profile–a Fermi function, given as follows

$$y_n(\xi) = c - \frac{c - u}{\exp(\xi/\hat{\xi}) + 1} \tag{50}$$

$$\rho_n(\xi) = \rho_{n0} + \frac{\rho_{n1} - \rho_{n0}}{\exp(\xi/\hat{\xi}) + 1} \tag{51}$$

where $\hat{\xi}$ defines the shock width, which is usually on the order of 14 neutral-neutral mean free paths. This restriction, however, still prevents the charged component from affecting the neutral component. He also removed the assumption that $V_i^2/v_{ia}^2 \ll 1$, which allows for stronger shocks. With these assumptions, Equation 39 becomes

$$\frac{dy_i}{d\xi} = \frac{\nu_{in}(y_i - y_n(\xi))y_i}{y_i^2 - v_{ia}^2} \tag{52}$$

This equation yields smooth solutions of the charged component velocity and density. From these, Equation 48 yields a smooth electric field estimate through the shock. The continuous electric field allows the derivation of the net charge density in the vicinity of the neutral shock front by way of Poisson's equation, Equation 2.

These extensions require a numerical solution. Equation 52 was solved using a fourth-order Runge-Kutta routine. The collision frequency is given by Equation 29. Figure 9 depicts the charged component velocity. The charged component density is shown in Figure 10. Note that the numerical and analytical solutions show only minor deviations for the parameters used. The electric field is depicted in Figure 11. A charged particle passing through this field would experience a potential drop of $-1.5\,\mathrm{V}$, which is in good agreement with the analytical treatment. Finally, Figure 12 illustrates the separation of charge that occurs at the shock front. The electrons are broadly distributed through the precursor due to their high mobility, while the ions are compacted at the shock front due to the strong electric field and their low mobility.
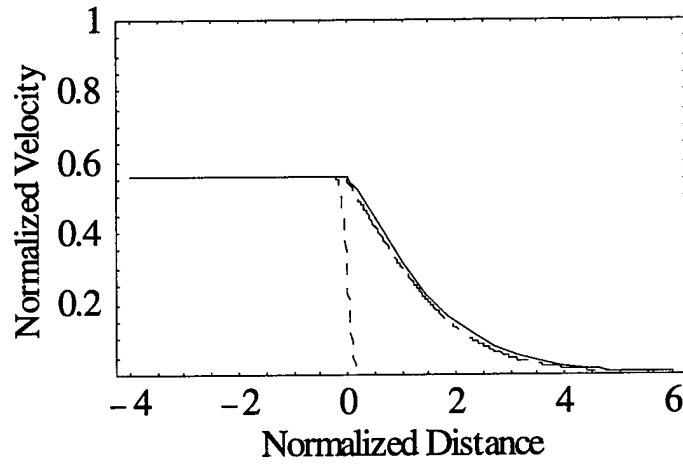
Figure 9   Steady state numerical solution of charged component velocity (broad dashes) for a Mach 2 shock in argon.   Analytic solution (solid) and neutral velocity (short dashes) shown for comparison. Velocity is normalized to the shock velocity, c.   Distance is normalized by $\xi_0 = 3.4\,\mathrm{mm}$.
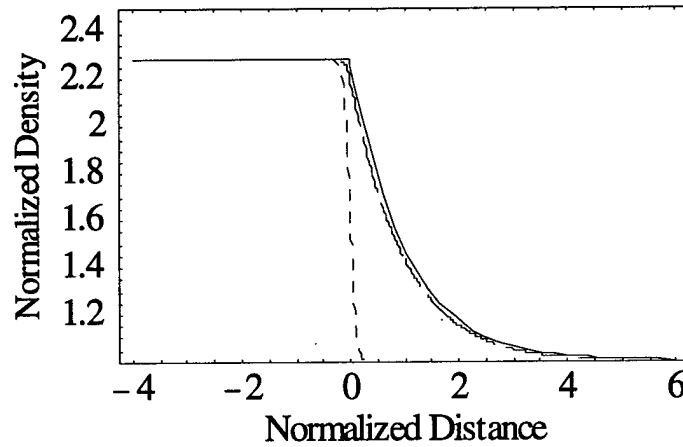
Figure 10   Steady state numerical solution of charged component density (broad dashes) for a Mach 2 shock in argon.   Analytic solution (solid) and neutral density (short dashes) shown for comparison. Densities are normalized to upstream values.   Distance is normalized by $\xi_0 = 3.4\,\mathrm{mm}$.
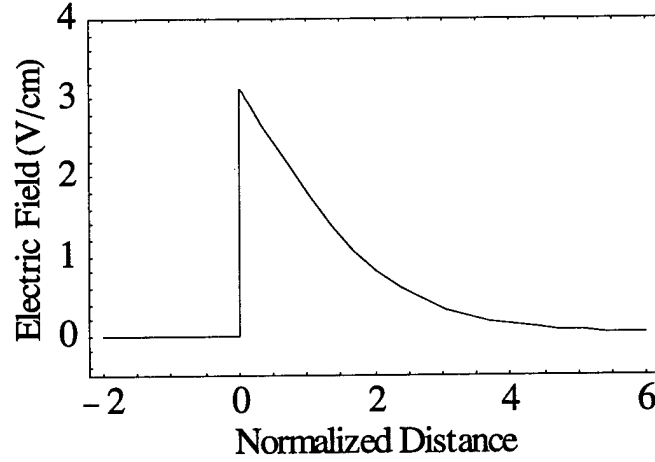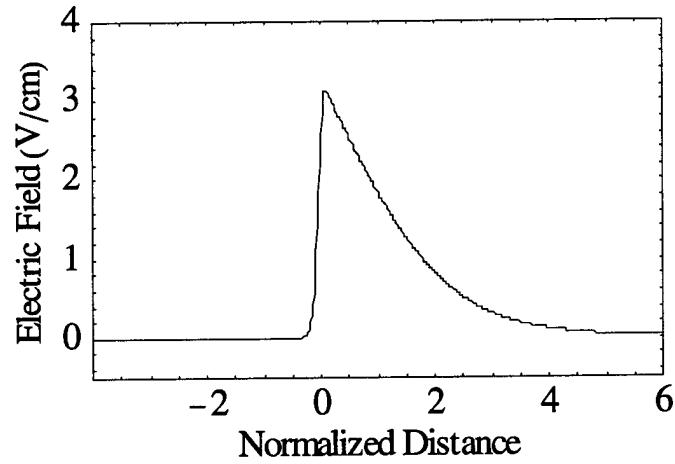
Figure 11   Steady state numerical solution of the electric field in the vicinity of a Mach 2 shock in argon.   Distance is normalized by $\xi_0 = 3.4\,\mathrm{mm}$.
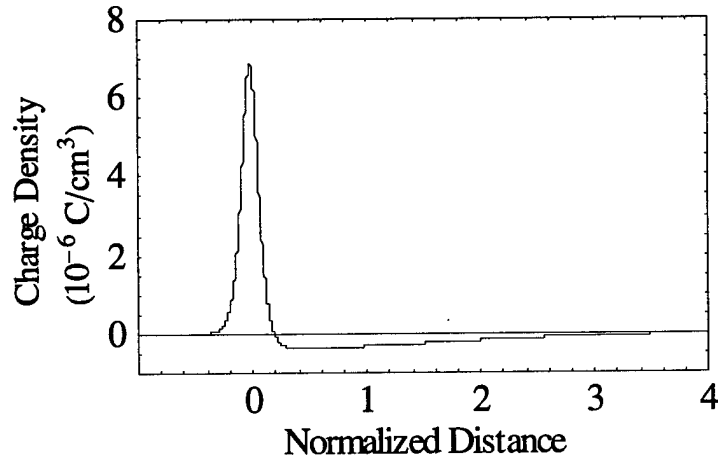
Figure 12   Steady state numerical approximation of the net charge density in the vicinity of a Mach 2 shock in argon.   Distance is normalized by $\xi_0 = 3.4\,\mathrm{mm}$.   Electronic double layer is clearly visible.

30

3.2 Time-dependent

Hilbun's development continues with a time-dependent approach. In his treatment of shock propagation, he examined three facets of weakly ionized gases–a vibrationally excited gas, a hot gas, and a plasma–and developed numerical solutions for each case (22:25). In the case of the vibrationally excited gas, Hilbun assumed the gas is a non-equilibrium store of vibrational energy. The objective was to determine the amount of vibrational energy that is transferred to translational energy as the shock passes through it. For the hot gas approximation, Hilbun used a two dimensional fluid dynamics code to investigate the modifications on the shock propagation parameters as it passes through thermal inhomogeneities. The present research focuses on the plasma aspect of the weakly ionized gas.

3.2.1 One dimensional, two-fluid approximation. Hilbun's approach to modelling the medium is also a two-fluid approximation–neutrals and charged particles, where the electrons are assumed to be steady-state. Therefore, the electric field can be derived from the steady state electron momentum equation, and is given by Equation 48. The treatments reviewed in the previous section assume static neutral density, velocity, and temperature profiles; however, the present approach allows for modification of the neutral flow. Interaction between the fluids occurs through energy and momentum coupling and there are no production or loss mechanisms. Viscosity and thermal conductivity are assumed to be negligible, which allows Euler's equations to be used instead of the complex Navier-Stokes equations. Therefore, the neutral profiles, and those of the charged component, are determined by solving Euler's equations.

Hilbun's time-dependent equations take on the following form (22:79):

$$\frac{\partial \overline{U}}{\partial t} + \frac{\partial \overline{F}}{\partial x} = \overline{S}_1 + \overline{S}_2 + \overline{S}_3 \qquad (53)$$

31

where the terms on the left are the derivatives of the conserved variables–mass, momentum, and energy–and the terms on the right are called source terms–sources of mass, momentum, and energy. The specific vectors are defined below. The vector of conserved variables, $\overline{U}$, is defined as

$$
\overline{U} = \begin{bmatrix} \rho_n \\ \rho_n V_n \\ \rho_n(\frac{1}{2}V_n^2 + \frac{1}{1-\gamma}\frac{k_B T_n}{m}) \\ \rho_i \\ \rho_i V_i \\ \rho_i(\frac{1}{2}V_i^2 + \frac{1}{1-\gamma}\frac{k_B T_i}{m}) \end{bmatrix}
\tag{54}
$$

The flux vector, $\overline{F}$, is defined as

$$
\overline{F} = \begin{bmatrix} \rho_n V_n \\ \rho_n V_n^2 \\ \rho_n V_n(\frac{1}{2}V_n^2 + \frac{1}{1-\gamma}\frac{k_B T_n}{m}) \\ \rho_i V_i \\ \rho_i V_i^2 \\ \rho_i V_i(\frac{1}{2}V_i^2 + \frac{1}{1-\gamma}\frac{k_B T_i}{m}) \end{bmatrix}
\tag{55}
$$

The source terms for the Euler equations and species coupling are given by the following:

$$
\overline{S}_1 = -\frac{\partial}{\partial x}\begin{bmatrix} 0 \\ P_n \\ P_n V_n \\ 0 \\ P_i \\ P_i V_i \end{bmatrix}, \quad \overline{S}_2 = \begin{bmatrix} 0 \\ P_{ni} + P_{ne} \\ Q_{ni} + Q_{ne} \\ 0 \\ -P_{ni} \\ -Q_{ni} - Q_{ei} \end{bmatrix}
\tag{56}
$$

where P_{jk} represents the momentum gained by species j at the expense of species k, and Q_{jk} represents a similar transfer of energy between the two species. The momentum transfer between ions and electrons is zero by definition since their velocities are assumed to be equal in the two-fluid approximation. Jaffrin (23:611) gives the specific momentum and energy coupling terms as

$$P_{ni} = \frac{4}{3} n_n n_i \sigma_{in} (V_i - V_n) \sqrt{\frac{2m}{\pi} k_B (T_n + T_i)} \tag{57}$$

$$P_{ne} = \frac{8}{3} n_n n_e \sigma_{en} (V_i - V_n) \sqrt{\frac{2m_e k_B T_e}{\pi}} \tag{58}$$

$$Q_{ni} = 2 n_n n_i \sigma_{in} \sqrt{\frac{2}{\pi m} k_B (T_n + T_i)} \{ k_B (T_n - T_i) + \frac{1}{3} m (V_i - V_n)(V_i + V_n) \} \tag{59}$$

$$Q_{ne} = 8 n_n n_e \sigma_{en} \sqrt{\frac{2m_e k_B T_e}{\pi}} \{ \frac{k_B}{m} (T_e - T_n) + \frac{1}{3} (V_i - V_n)(V_n + \frac{m_e}{m} V_i) \} \tag{60}$$

$$Q_{ei} = 8 n_i n_e \sigma_{ei} \frac{k_B}{m} (T_i - T_e) \sqrt{\frac{2m_e k_B T_e}{\pi}} \tag{61}$$

The electric field source term is given by

$$\overline{S}_3 = -\frac{k_B T_e}{m} \frac{\partial \rho_i}{\partial x} \begin{bmatrix} 0 \\ 0 \\ 0 \\ 0 \\ 1 \\ V_i \end{bmatrix} \tag{62}$$

where the electric field, E, is approximated by Equation 48.

Hilbun's numerical techniques involve a finite difference, second order accurate MacCormick algorithm with flux corrected transport (FCT). The MacCormick method is widely used in solving fluid flow equations (3:102). It is a predictor-corrector method, in which the predictor term uses forward differencing and the corrector term uses backwards differencing. This differencing can be reversed for cases involving moving discontinuities, such as shocks. The FCT algorithm rids the solution of oscillations resulting from second order algorithms. The algorithm advances the solution by a time step in a two-step process (38:84). In each half-step, a diffusive flux is applied to the solution to introduce numerical diffusion to ensure stability and monotonicity, and then an anti-diffusive flux is applied to eliminate excessive numerical flux.

In order to compare the solution obtained with Hilbun's plasma code to Avramenko's solution, a Mach 2 test case was completed. The initial conditions $P_4/P_1 = 22.2$ and $T_4/T_1 = 2.0$ generate a Mach 2 shock in a shock tube, as determined by Equation 19. Hilbun's time-dependent code accurately solves the Riemann problem, as illustrated in Figure 13 (compare to Figure 4), though there were no modifications to neutral shock structure and propagation. The time-dependent solution matches Avramenko's results in that a charged precursor appears before the shock, as shown in Figure 14. The solution also yields an electric field near the shock, as shown in Figure 15. Though the field may be broader and less intense than the field obtained with the steady-state approach, a charged particle passing through this field would also experience a potential drop of $-1.5\,\text{V}$. Net charge density is approximated by Equation 2 and is illustrated in Figure 16; the EDL is clearly visible, though the ionic portion of the EDL is far less concentrated than in the steady state case (compare to Figure 12). Since this approach assumes charge neutrality, the globally integrated charge density should sum to zero. Letting the numerical error be measured with the respect to the maximum charge density in Figure 16, charge neutrality is main-

34
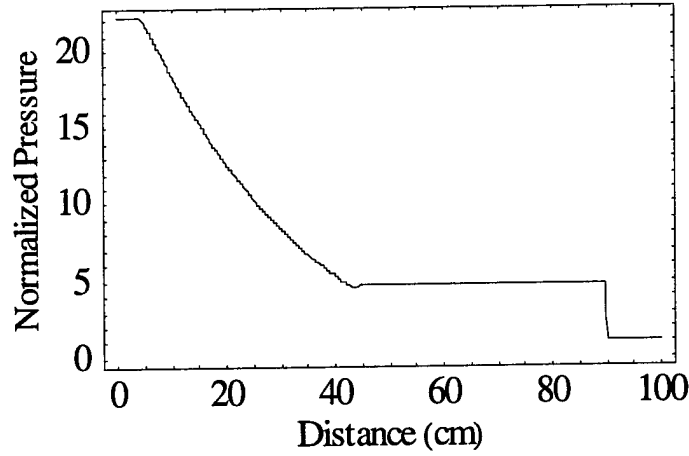
Figure 13   Hilbun's one-dimensional plasma code solution of neutral pressure for a
Mach 2 shock in argon. Shock and expansion waves are clearly visible.

tained to within 98.8 percent. The magnitude of this error is due in part to the
coarseness of the spatial grid used in the numerical solution.

There are two minor concerns when using Hilbun's plasma code. First, mo-
mentum and energy coupling between the heavy particles and electrons must be
neglected. Coupling is afforded in the code via Equations 58, 60, and 61. Since the
electron temperature is assumed constant, the electron coupling terms provide an
unlimited source of energy for the heavy particles as T_n and T_i equilibrate with T_e.
Therefore, in two-fluid calculations, it is best to neglect electron coupling by setting
σ_{ei} and σ_{en} to zero. Secondly, using an average, order of magnitude approximation
of the ion-neutral collision cross section, $\sigma_{in} = 10^{-19} \, \mathrm{m}^2$, causes numerical instabil-
ities. The code requires a cross section that is 25 times smaller than this value
(22:89). This is most likely due to the fact that the average time step in the calcula-
tion, $\Delta t \sim \Delta x / v_{ia}$, is larger than the ion-neutral collision time, $\tau_{in} \sim 1/\sqrt{2} n_n \sigma_{in} V_i$.
Assuming an average σ_{in} of $10^{-19} \, \mathrm{m}^2$ and test conditions of $T_e = 2 \, \mathrm{eV}$, $T_i = 300 \, \mathrm{K}$,
and $P_{n0} = 30 \, \mathrm{torr}$, the ratio $\Delta t / \tau_{in}$ is on the order of 10^2. Nominal values of σ_{in}
could be used if the computational time step is reduced by two orders of magnitude.
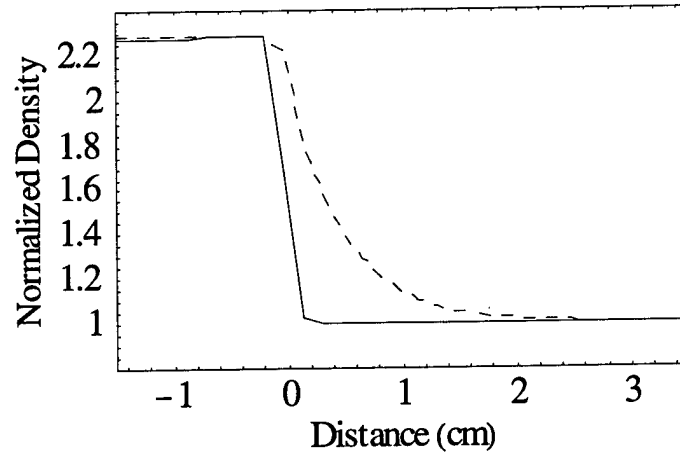
Figure 14   Solution of charged component density (dashed) for a Mach 2 shock in argon. Neutral density (solid) shown for comparison. Densities are normalized by upstream values.
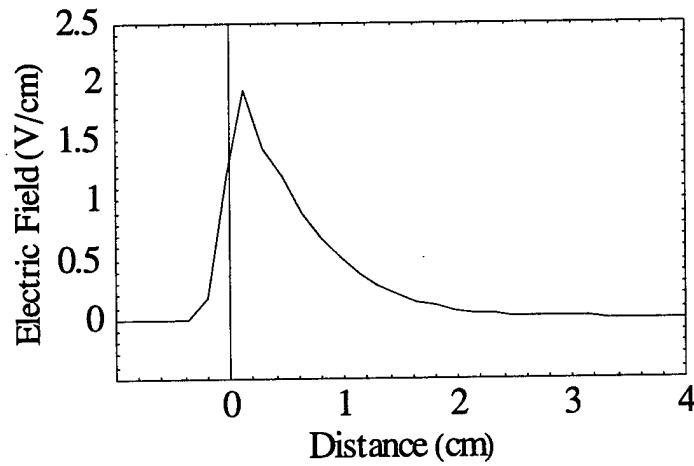
Figure 15   Approximation of electric field for a Mach 2 shock in argon.

36
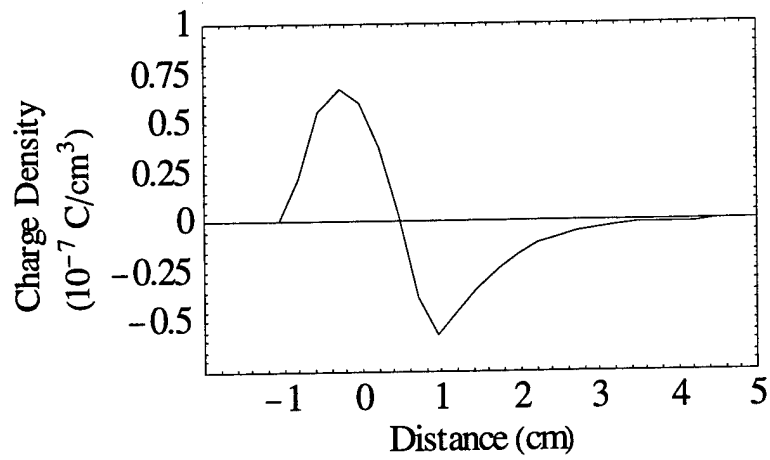
Figure 16   Approximation of net charge density for a Mach 2 shock in argon.

Unfortunately, the time and computational restraints levied upon this research effort precluded the use of these more accurate calculations.

IV. Lifted Restrictions

According to Hilbun (22:96), in order for ion-acoustic wave damping to affect the neutral flow, two conditions must be met: 1) The ion-acoustic wave energy density must be an appreciable fraction of the neutral energy density, and 2) the time scale for the energy transfer from the ion-acoustic wave to the neutral flow must be less than the transit time for a neutral particle to pass through the charged component precursor. Hilbun derives the threshold fractional ionization, α_{ia}, that meets these two criteria: $\alpha_{ia} \geq 5 \times 10^{-3}$. Figure 17 illustrates the effect of ion-neutral momentum coupling. Various fractional ionizations were tested using the same initial conditions, $P_4/P_1 = 10.0$ and $T_4/T_1 = 1.25$ [1]. The horizontal line represents shock speed that is unaffected by the presence of the plasma, and the vertical line represents Hilbun's value of α_{ia}. Shock acceleration due to ion-acoustic damping is clearly visible for Hilbun's value of α_{ia}, but the results of his time-dependent solution seem to favor $\alpha_{ia} \simeq 1 \times 10^{-3}$ as the threshold.

According to Adamovich, et al. (1:816), and Jaffrin (23:610), gaseous media with $\alpha \simeq 10^{-3}$ are generally classified as *partially* ionized gases, which are not considered within the scope of this research. However, if the value of α of a weakly ionized gas were to increase to partially ionized values in the *vicinity* of the shock, then ion-acoustic wave damping may be effective in altering shock structure and propagation. A possible mechanism for varying the fractional ionization at the shock front, α_S, is additional ionization. Recall the modified ion momemtum equation from the previous chapter (Equation 24):

$$\frac{\partial}{\partial t}(\rho_i V_i) + V_i \frac{\partial}{\partial x}(\rho_i V_i) = -\nabla P_i + \frac{\rho_i q E}{m} - \rho_i \nu_{in}(V_i - V_n)$$

---

[1] These initial conditions will be used for the remainder of the work. Unless otherwise stated, all plasma code solutions assumed a shock tube length of 1 m, with the diaphragm located at $x = 0.4$ m, and all shocks propagated to $x = 0.9$ m.
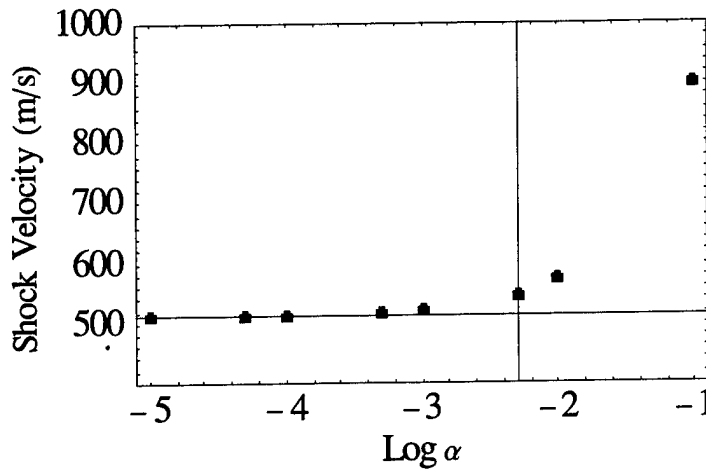
Figure 17   Neutral shock propagation speed vs. fractional ionization, α. The vertical line indicates the threshold fractional ionization, α_{ia}, for effective ion-acoustic wave damping as derived by Hilbun. The horizontal line indicates nominal shock velocity in an unionized gas.

Both the pressure gradient and electric field forces act in the direction of shock propagation. It was made plain by Figure 15 that there is a positive electric field at the shock front. These forces work to increase the ion velocity above the neutral velocity. As the ion velocity increases, however, collisional coupling with the neutrals restricts the forward movement of the ions. Because of this, a large portion of the ions generated at the shock front will tend to remain there. As the ion density builds at the shock, it could reach a level conducive to momentum transfer to the neutrals via ion-acoustic wave damping.

In Hilbun's conclusion on plasma effects (22:96), he states that in his time-dependent solution, "Under plasma conditions typically encountered in glow discharges, the charged particles are observed to have practically no influence on the density, velocity, and temperature of the neutral component in the parameter space investigated. The neutral shock velocity also remained unaffected by the plasma component under these conditions." The field strength was comparable to the axial field of a glow discharge, but was of such small spatial extent that electrons were

39

not significantly affected (22:75). Hilbun's argument against additional ionization is this: The peak electric field at the shock front is of the same order of magnitude as the axial electric field typically found in a glow discharge in argon at 30 torr, about 50 V / cm. However, the field is localized to a small region around the shock front; therefore, the total potential drop is only on a few Volts. With electron thermal energies of about 2 eV, this potential drop falls short of ionization potential of argon, $I_P = 15.8$ eV (40:389), and is unable to significantly increase ionization at the shock front.

The logical extrapolation of this argument is that stronger electric fields and greater precursor widths should lead to greater potential drops for electrons. These conditions could be generated by elevated electron temperatures at the shock front. The resulting potential drops could approach the ionization potential of argon. Adopting a quasi-kinetic approach, for the given average thermal energy of the electrons (about 2 eV) a small fraction of the electrons will have energies greater than I_P. This fraction, albeit small, is 3.7×10^{-4} and is given by the Boltzmann factor, $\exp(-I_P/k_B T_e)$. If the ion density builds over time, ion-neutral momentum coupling could begin to play a significant role in shock structure and propagation via ion-acoustic wave damping, which was mentioned in Section 2.2.2.

It may seem intuitous that larger amounts of plasma would generate larger electric fields due to the greater numbers of charged particles that constitute the charge separation. This, however, is not the case. From the previous chapter, the electric field approximation is given by

$$E \approx -\frac{k_B}{\rho_i e}\frac{d(\rho_i T_e)}{d\xi} = -\frac{k_B}{e}\left(\frac{T_e}{n_i}\frac{dn_i}{d\xi} + \frac{dT_e}{d\xi}\right) \qquad (63)$$

The electric field is directly related to the charged component pressure gradient, in which the electron thermal energy and its spatial gradient, and the spatial gradient of the ion density are all factors. More energetic electrons and stronger shocks
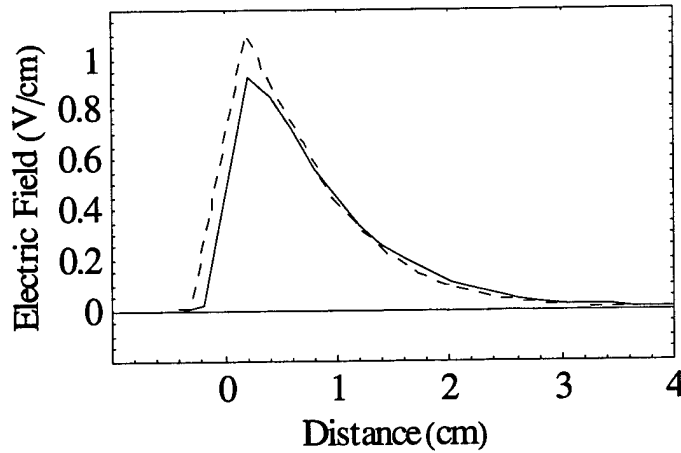
Figure 18   Comparison of electric fields for $\alpha = 10^{-2}$ (solid) and $\alpha = 10^{-6}$ (dashed). Charged particles in each of these fields experience a potential drop of only -1V.

will generate stronger electric fields.   The field is independent of the actual ion density, however.   As α increases, the electric field and potential remain relatively unchanged, which is the case in Figure 18.   For both values of α represented, the associated electric fields both produced potential drops on the order of $-1\,\mathrm{V}$.   Also, as α increases, the charge separation and net charge density are relatively unchanged, as seen in Figure 19.   Yet, in Figure 17, the cases in which $\alpha \geq 1 \times 10^{-3}$, the shocks propagated at velocities in excess of the unionized Riemann case.   This indicates that ion-neutral momentum coupling is the critical factor in the modification of neutral shock structure and propagation.   The required increase in ion density, however, can not come about unless the electric potential is of sufficient strength to enhance electron impact ionization.   The field strength, of course, is a function of the electron energy at the shock front.

It is the intent of this research to extend the investigation of the structure and propagation of shocks in weakly ionized gas as the EDL is freely affected by variable electron temperature and additional electron impact ionization at the shock.   Greater ion-neutral coupling, assisted by a stronger electric field and potential, could provide

41
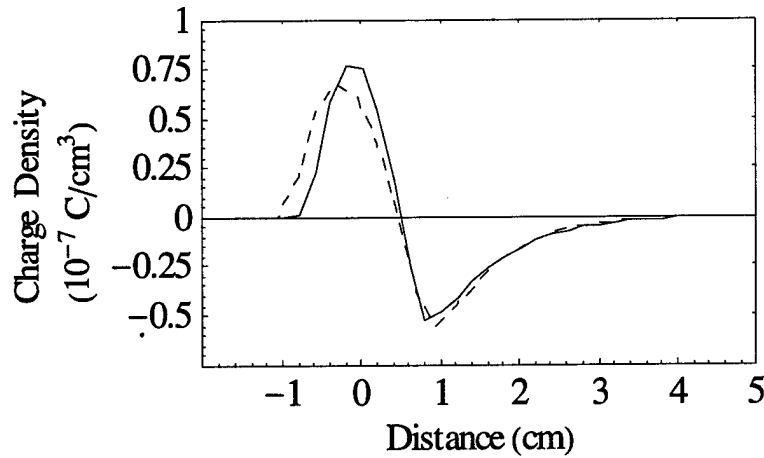
Figure 19   Comparison of net charge density profiles for $\alpha = 10^{-2}$ (solid) and $\alpha = 10^{-6}$ (dashed).

the means for shock modification in weakly ionized gases.   A spatially-dependent electron temperature will enhance the strength and breadth of the electric field, as evident in Equation 63.   The enhancements in electron temperature will sustain ionization at the shock front by increasing the energies of free electrons.   This chapter investigates these mechanisms.   Each of the following sections are divided into the development of the lifted restriction, a description of the results, and an analysis of the results.

4.1   Variable electron temperature

4.1.1   Development.   Recent research by Sirghi, et al., (36), indicates that electron temperatures increase in the vicinity of a strong electric field.   The goal of their research was to determine the distribution function of electrons at sharp changes in diameter in glow discharge tubes.   In their working media of helium at 1 torr, large electric fields were generated at these constrictions, with values two to four times the ambient homogeneous positive column electric field.   With an homogeneous field in DC positive column of about 4 V / cm, the induced field experienced a maximum of approximately 11 V / cm ahead of the constriction, and had a

42
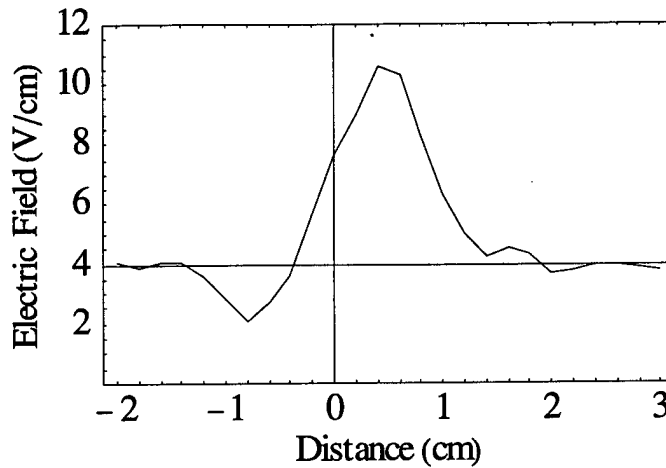
Figure 20   Electric field vs. distance. Rise in field was generated by a constriction in a glow discharge tube. Field structure is similar to that experienced at a shock in weakly ionized gas (Ref: (36). Note that geometry has been reversed).

width of approximately 1 cm. This field structure is illustrated in Figure 20, where the mouth of the constriction resides at $x = 0$, and the constricted region is where $x < 0$. This induced field is not unlike the electric field generated by the EDL at a shock front in a weakly ionized gas. In the region of elevated electric field, ambient electron energies of approximately 5 eV were nearly doubled as seen in Figure 21. Sirghi attributed the increased electron energy to the induced electric field. It is clear from Equations 58, 60, and 61 that momentum and energy coupling with the heavy particles cannot account for the distributions, since this would only heat the heavy particles and lower the energies of the electrons due to equilibration. Even though the research cited here involves weakly ionized helium, similar phenomena should be expected in argon as well.

The restriction of constant electron temperature was lifted by incorporating a spatially-dependent region of electron heating in the vicinity of the neutral shock front. This region was similar in form to the electron thermal layer evident in Figure 21 and, for simplicity, took the form of a shock-centered Gaussian rise in electron

temperature over and above the baseline electron temperature, T_{e0}:

$$T_e(\xi) = T_{e0} + \Delta T_e \exp(-(\frac{\xi}{\delta\lambda})^2) \tag{64}$$

where ΔT_e is the increase in electron temperature, usually a fraction of T_{e0}, and δ
is the number of upstream mean free paths, λ, that specify the approximate half-
maximum width of the Gaussian curve. ΔT_e and δ serve as the coordinates of the
parameter space investigated. The mean free path is given by (17:95) as:

$$\lambda = \frac{1}{\sqrt{2}n_{n0}\sigma_{in}} \tag{65}$$

where n_{n0} is the upstream neutral number density and σ_{in} is the ion-neutral collision
cross section.

The central assumption of the two-fluid approximation was that of steady-
state electron momentum. It might seem that the incorporation of a spatially-
dependent electron temperature would violate this assumption. It is important to
note that the assumption is not violated. Consider Equation 53 and its constituent

44

vectors as a basis. On the source side of the equation, if the collisional coupling of the electrons is ignored, then the momentum is maintained by a balance between the pressure gradient and the force imparted by the electric field. The variable temperature introduces a temperature gradient term in the pressure gradient, which is compensated also by a temperature gradient term in the electric field. On the conserved variable side, changes in density must be maintained by changes in fluid velocity. Furthermore, the conservation of energy is maintained as well. For the source side of Equation 53, a balance between the pressure gradient and the electric field term similar to that described above holds here as well. On the left side, a balance between electron temperature, density, and fluid velocity is maintained. Of note, however, is the fact that the strengths and spatial extents of the electron thermal layer are based on empirical results rather than a solution of the electron continuity, momentum, and energy equations. Temperature increases and gradients that are too large may lead to nonphysical solutions of density and velocity.

The spatially-dependent electron temperature was easily incorporated into Hilbun's two-fluid plasma code. A simple subroutine employing Equation 64 was implemented. The value of λ was calculated in the code in accordance with Equation 65, the parameters ΔT_e and δ were user-supplied, and the shock location, $\xi = 0$, was determined in the code for each time step. In addition to the $T_e(\xi)$ modification, the electric field source term, $\overline{S_3}$, was modified to account for the variable electron temperature:

$$\overline{S_3} = -\frac{k_B}{m}\frac{\partial}{\partial x}(\rho_i T_e) \begin{bmatrix} 0 \\ 0 \\ 0 \\ 0 \\ 1 \\ V_i \end{bmatrix} \tag{66}$$

45
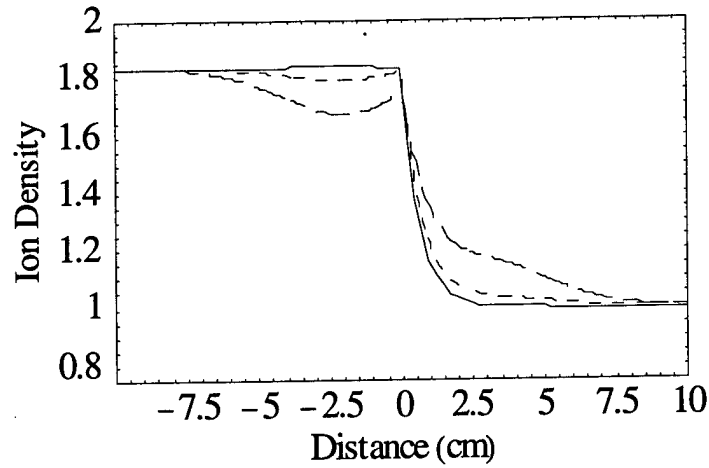
Figure 22   Normalized ion density profiles resulting from variable electron temperature. Constant $T_e = 2\,\text{eV}$ (solid line), $\Delta T_e = 1\,\text{eV}$ (short dashes), and $\Delta T_e = 2\,\text{eV}$ (broad dashes).

4.1.2 Results.   Incorporating the spatial variation of the electron temperature led to three effects on the charged component flow parameters and electric field structure. The first was an increase in the charged component precursor width, ξ_0. This increase in precursor width is illustrated in Figure 22, where the solid line represents the normalized ion density of the constant $T_e = 2\,\text{eV}$ case, the short dashes represent $\Delta T_e = 1\,\text{eV}$, and the broad dashes represent $\Delta T_e = 2\,\text{eV}$. The second and third, in association with the first effect, were a general broadening and strengthening of the electric field and a variation in the charge distribution around the shock front. Figure 23 illustrates the variation in the electric field; the solid line represents the constant $T_e = 2\,\text{eV}$ case and the dashed line represents the $\Delta T_e = 2\,\text{eV}$ case. Figure 24 illustrates the net charge density, which was approximated via Equation 2. In this case, charge neutrality is maintained to within 98.6 percent. Again, as in the previous chapter, the magnitude of the error is due in part to the coarseness of the spatial grid used in the numerical solution. For all values of ΔT_e and δ investigated there were no significant effects on neutral flow variables, shock structure, or shock propagation, which is expected from the arguments in the beginning of the chapter.

46
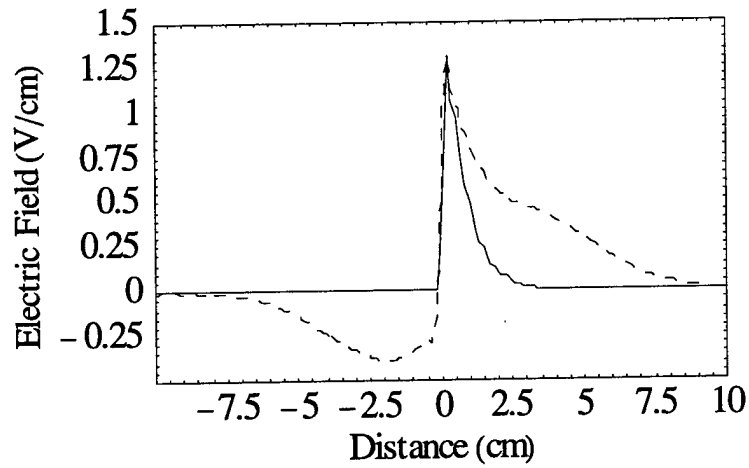
Figure 23   Electric field variation resulting from variable electron temperature. Constant $T_e = 2\,\mathrm{eV}$ (solid line) and $\Delta T_e = 2\,\mathrm{eV}$ (dashes).
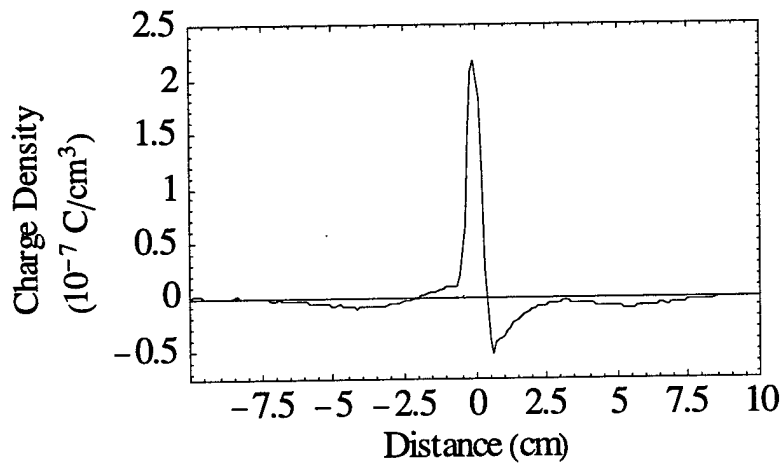
Figure 24   Approximate net charge density resulting from variable electron temperature. $\Delta T_e = 2\,\mathrm{eV}$ and $\delta = 200$.

4.1.3 Analysis. The increase in precursor width is simply the result of capturing the local value of T_e. As an illustration, recall Avramenko's definition of the steady-state precursor width, Equation 45:

$$\xi_0 = \frac{v_{ia}^2}{c v_{in}} = \frac{k_B T_e}{m c \nu_{in}}$$

The precursor width varies directly with electron temperature and the precursor exists in this region of elevated electron temperature.

The profile of the electric field is affected by the variable electron temperature. Recall Equation 63:

$$E \approx -\frac{k_B}{q}\left(\frac{T_e}{n_i}\frac{dn_i}{d\xi} + \frac{dT_e}{d\xi}\right)$$

When Equation 64 is subsituted for T_e, the equation becomes

$$E \approx \frac{k_B}{q}\left(-\frac{T_e(\xi)}{n_i}\frac{dn_i}{d\xi} + \frac{2}{\delta\lambda}\xi\exp(-(\frac{\xi}{\delta\lambda})^2)\right) \tag{67}$$

The term on the left is generally positive, but only has a significant value near $\xi \simeq 0$. The term on the right is positive for $\xi > 0$, and negative for $\xi < 0$, which creates the negative portion of the electric field. For $\xi \ll 0$ and $\xi \gg 0$, $d\rho_i/d\xi$ and the exponential term are both essentially zero, and the field vanishes. In Figure 23 the broad negative region behind the shock draws ions away from the shock front, further reducing the possibility of effective ion-acoustic wave damping. The broad positive field region imparts energy to the ions and extracts energy from the electrons, but the ion-neutral coupling at this fractional ionization is not strong enough to affect the neutral population. The variation in ion density illustrated in Figure 22 shows the influence of this field, particularly in the partially evacuated region just behind the shock. The total potential drop over the region is about $-2\,\text{V}$; however, since net ion production is still restricted, efficient coupling between the ions and neutrals does

48

not occur and the neutral flow remains unaffected. Of particular note, the profile of the numerical solution to the electric field resembles the observed profile in Sirghi's research, depicted in Figure 20, including a depressed region of the field for $\xi < 0$. This correlation between observation and the numerical results lends credence to the incorporation of a spatially-dependent electron temperature in Hilbun's code.

4.2 Electron Impact Ionization

4.2.1 Development. In a glow discharge, the plasma is generated by electron impact ionization, where electrons acquire energy from the applied electric field. Losses generally occur through diffusion to the walls of the tube. As stated in Chapter I, the present research focuses on a one-dimensional approximation; therefore, two-dimensional, radial loss processes cannot be considered. The production and loss of plasma are assumed to balance each other. This section investigates the effects of allowing additional ionization to occur at the shock front. Thus, the previous restriction of a zero net production mechanism is lifted. The growth in plasma density is only restricted by the energy present in the gas and by the assumed discharge geometry. Physical mechanisms to mitigate the ionization process are considered in the next section.

Even though Hilbun's plasma analysis does not allow for additional net ionization, he concedes that there is some experimental evidence that additional ionization is present at the shock front region: "If these measurements are accurate, then it may be possible for the fractional ionization in the shock front region to be significantly greater than that normally present in the quiescent plasma in front of the shock. In such a case, energy transfer from the ion-acoustic wave to the neutral shock may become a relevant process, resulting in a perturbation of the neutral flow (22:98)." The research to which he refers was conducted by Gorshkov, et al., (19), and Chutov (13).

From work Chutov had completed in the 1970s, he discovered that "a shock wave in a gas-discharge plasma changes the degree of its ionization at any [shock] intensity." It has been shown that the presence of the electronic double layer due to the steep gradients at the shock creates a potential drop. When the direction of the field due to the double layer coincides with that of the electric field in the discharge, then additional energy is released in the region of the potential drop, which leads to additional ionization at the front. Gorshkov coined this effect as an "electric detonation" (13:506).

Gorshkov detected additional ionization at the shock front in decaying glow discharges. Shock propagation and structure were measured in the discharges of a variety of gases–Ar, N_2, and CO_2. The absence of an ambient electric field during passage of the shock is similar to the conditions incorporated into the model used in the present research. Using collimated photomultipliers, they measured the emissions of the glow discharge plasma and observed a significant drop in luminosity at the shock, which they attributed to stimulated ionization of excited particles at the shock front (19:1141).

The present research will assume a quasi-kinetic approach to additional ionization at the shock front. The number of ionization events per unit volume per unit time is a simple result of kinetic theory assuming a Maxwellian distribution (e.g. see (40:386)):

$$Z_{ion}^e = (\frac{dn_e}{dt})_{ion} = n_n n_e \int_{v_k}^{\infty} \sigma_e(v_e) v_e f_e(v_e) dv_e = n_n n_e k_e \qquad (68)$$

where v_e is the electron thermal velocity, $\sigma_e(v_e)$ is the electron impact ionization cross section, and $f_e(v_e)$ is the electron velocity probability function. The integration extends over electron thermal speeds whose energies exceed the ionization potential; therefore the lower limit of integration is $v_k = \sqrt{2I_P/m_e}$. Even though $\sigma_e(v_e)$ is a function of electron energy, for the purpose of approximation it is assumed to

be roughly constant. For all cases, σ_e was given an order of magnitude estimate of $10^{-21}\,\text{m}^2$. The Maxwellian velocity distribution, $f_e(v_e)$, is assumed to be one-dimensional. Therefore, the ionization coefficient, k_e, evaluates to

$$
\begin{aligned}
k_e &= \sigma_e \int_{\sqrt{2I_P/m_e}}^{\infty} v_e \left(\frac{m_e}{2\pi k_B T_e}\right)^{1/2} \exp\left(-\frac{m_e}{2k_B T_e} v_e^2\right) dv_e \\
&= \frac{\sigma_e}{\sqrt{2\pi}} \sqrt{\frac{k_B T_e}{m_e}} \exp\left(-\frac{I_P}{k_B T_e}\right) \qquad (69)
\end{aligned}
$$

The ionization coefficient then is simply a function of electron temperature. In this investigation, the electron temperature is defined by Equation 64. The quantity I_P/k_B in the Boltzmann factor can be considered as an ionization temperature, T_P. With an ionization potential of 15.8 eV for argon, T_P evaluates to 1.83×10^5 K. This eliminates consideration of ionization by ion-neutral and neutral-neutral collisions. Since these particles have temperatures on the order of 300 K, the heavy particle Boltzmann factor is essentially zero. Free electrons, however, yield more substantial ionization coefficients. For $\Delta T_e/T_{e0}$ as low as 0.02, the ionization coefficient due to electron impact, k_e, is about $1.1 \times 10^{-13}\,\text{cm}^3/\text{s}$. For ambient initial conditions of $n_{n0} = 5.5 \times 10^{18}\,\text{cm}^{-3}$ and $\alpha = 10^{-6}$, the ionization rate is about $3.2 \times 10^{12}\,\text{cm}^{-3}\,\mu\text{s}^{-1}$. The average computational time step in the plasma code is within an order of magnitude of $1\,\mu$s; therefore, within one time step, a 60 percent increase in the ion density at the shock would be expected.

A similar ionization rate as that above could be derived for the ambient electron temperature (2 eV or 23200 K); therefore, the ionization terms must be balanced or nullified in the regions away from the shock. This balance was struck by using the following relationship:

$$
\left(\frac{dn_e}{dt}\right)_{net} = Z_{net} = n_n n_e (k_e - k_{e0}) \qquad (70)
$$

51

in which

$$k_{e0} = \frac{\sigma_e}{\sqrt{2\pi}} \sqrt{\frac{k_B T_e}{m_e}} \exp(-\frac{I_P}{k_B T_{e0}}) \tag{71}$$

Therefore, the net ionization rate is simply a function of the difference in the exponential terms. Away from the shock, where $T_e = T_{e0}$, then $Z_{net}^e = 0$.

Due to the dependence on Equation 64, the electric field should retain the basic characteristics of the field generated in the previous section (Figure 23). Since the region of ionization is assumed to be centered on the shock due to its dependence on Equation 64, a large number of the freed electrons would tend to accumulate at the shock. An argument was presented at the beginning of the chapter that promulgated the idea that the newly created ions would generally remain at the shock front. As the ion density builds at the shock, a large number of electrons should be expected to remain in the vicinity of the shock as well due to the mutual attraction of the ions and electrons. As a result of this accumulation of charged particles, an exponential increase in ion density in time is expected at the shock front, as determined by the differential equation, Equation 70. For the maximum electron temperature experienced, $T_e + \Delta T_e$, Equation 70 can be integrated to find $n_i(t)$ at the shock front, assuming quasi-neutrality, $n_i \simeq n_e$, applies:

$$\int_{n_{i0}}^{n_i} \frac{dn_i}{n_i} = \int_0^t n_n(k_e - k_{e0})dt \tag{72}$$

Since n_n is several orders of magnitude larger than n_i, n_n can be considered as a constant in the integration, as long as n_i only comes within a few orders of magnitude of n_n:

$$n_i(t) = n_{i0} \exp(n_n(k_e - k_{e0})t) \tag{73}$$

52

An estimate of the threshold value of ΔT_e required to produce a neutral shock acceleration can also be obtained. In the unionized Riemann problem, it takes the shock approximately $t_{Riemann} = 0.97\,\mathrm{ms}$ to propagate from $x = 0.4\,\mathrm{m}$ to $x = 0.9\,\mathrm{m}$. In order for the fractional ionization at the shock, α_S, to reach the fractional ionization required for effective ion-neutral momentum coupling, α_{ia}, within $t_{Riemann}$ the following condition must be met:

$$\exp(-\frac{I_P}{k_B T_e})\sqrt{\frac{k_B T_e}{m_e}}(1 - \exp(\frac{I_P}{k_B T_e} - \frac{I_P}{k_B T_{e0}})) - \frac{\sqrt{2\pi}}{\sigma_e}\frac{\ln(\alpha_{ia}/\alpha)}{n_n t_{Riemann}} = 0$$

where the ionization coefficients have been expanded. The condition yields $\Delta T_e/T_{e0} = 0.01$, or $\Delta T_e = 232\,\mathrm{K}$, as a lower limit to observe a neutral shock acceleration within the time limit, $t_{Riemann} = 0.97\,\mathrm{ms}$.

From Equation 73, it is possible to estimate the time for α_S to reach α_{ia}. Dividing both sides by n_{n0} and solving for t yields:

$$t_{ia} \simeq \frac{\ln(\alpha_{ia}/\alpha)}{n_n(k_e - k_{e0})} \tag{74}$$

For $\Delta T_e = 300\,\mathrm{K}$ and $\alpha = 10^{-6}$, the coefficients evaluate to $k_e = 9.76 \times 10^{-20}\,\mathrm{m^3/s}$ and $k_{e0} = 8.82 \times 10^{-20}\,\mathrm{m^3/s}$, which gives $t_{ia} \simeq 0.76\,\mathrm{ms}$.

Electron impact ionization was incorporated into Hilbun's one-dimensional plasma code in much the way that the variable electron temperature was. The ionization process is dependent upon the electron thermal layer at the shock; therefore, the variable electron temperature, Equation 64, was used. Incorporating additional ionization in Hilbun's code requires the modified electric field source term, Equation

66, and the introduction of a new ionization source vector:

$$\overline{S}_4 = \begin{bmatrix} -Z_{net}m_n \\ -Z_{net}m_nV_n \\ -Z_{net}m_n(\frac{1}{2}V_n^2 + \frac{1}{1-\gamma}\frac{k_BT_n}{m}) \\ Z_{net}m_i \\ Z_{net}m_iV_i \\ Z_{net}m_i(\frac{1}{2}V_i^2 + \frac{1}{1-\gamma}\frac{k_BT_i}{m}) \end{bmatrix} \tag{75}$$

4.2.2 Results and Analysis. For a range of the parameters $\Delta T_e/T_{e0}$ and δ, a number of test cases were completed for the initial conditions defined previously. Three trends were observed in neutral shock parameters, as exhibited in Figure 25. In the region indicated by the diamonds, there were negligible effects on neutral shock parameters; however, the electric field was strengthened and broadened. Total electric potentials grew to $-1.7\,\mathrm{V}$, indicative of the influence of the variation in electron temperature at the shock. In the parameter zone demarcated by the squares, steady accelerations of the neutral shocks were observed with an increase in electric field strength and width. Shock accelerations were observed for values of $\Delta T_e/T_{e0}$ just greater than the threshold determined above. Incidentally, shock acceleration generally occurred when the potential reached $-6\,\mathrm{V}$. There were also modifications of the neutral shock profile that could be interpreted as a weakening of shock strength. Perhaps the most intriguing result was the appearance of a significant neutral precursor, in the regime marked by the triangles. For convenience, a significant precursor is defined here as a 10 percent rise in upstream pressure in front of the shock. The strengths and spatial extents of the electron thermal layer employed in these test runs are based on empirical results rather than a solution of the electron continuity, momentum, and energy equations. Temperature increases and gradients that were too large led to nonphysical conditions and unstable solutions. The region indicated by the crosses represents these cases.

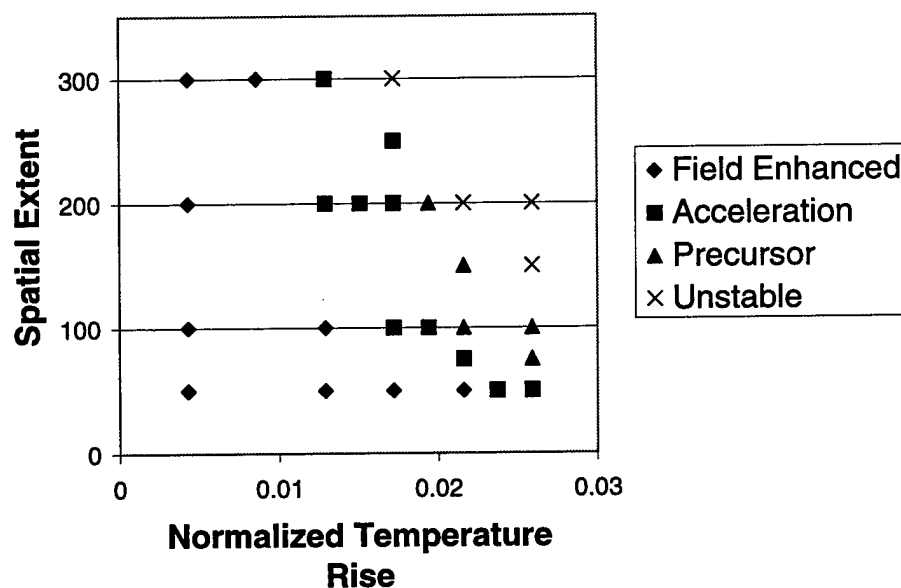Figure 25   Results of unrestricted electron impact ionization at the shock front. The parameter space is represented by the horizontal axis in terms of $\Delta T_e/T_{e0}$, and the vertical axis in terms of δ, measured in neutral-neutral mean free paths. Lower parameter values yielded strengthened and broadened electric fields. Higher values produced shock accelerations and neutral precursors.
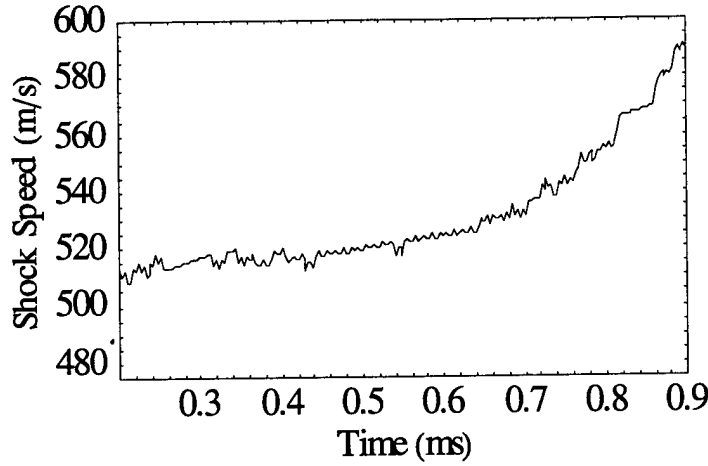
Figure 26   Acceleration of shock due to additional ionization.

Acceleration of the neutral shock was generally observed for $\Delta T_e \geq 300\,\mathrm{K}$ (for $T_{e0} = 2\,\mathrm{eV}$), just above the threshold value of ΔT_e derived above. The parameters of the case discussed below are $\Delta T_e = 300\,\mathrm{K}$ and $\delta = 300$. The acceleration begins at approximately $t = 0.45\,\mathrm{ms}$ after rupture of the diaphragm, as illustrated in Figure 26, which is about half the value of t_{ia} predicted by Equation 74 for $\Delta T_e = 300\,\mathrm{K}$. That prediction, however, did not take the width of the ionization region, δ, into account. If a linear velocity relationship is assumed over the time period of acceleration, the shock is seen to accelerate at approximately $1.4 \times 10^5\,\mathrm{m\,/\,s^2}$.

The neutral shock pressure and density profiles shown in Figures 27 and 28, respectively, do not match the profiles found in literature ((20), (27), (31), and (30)). Some distance behind the shock, there is a weakening in the pressure. Whereas the pressure ratio of the control case is 2.94, the lowest pressure ratio experienced in this region is $P_2/P_1 = 2.22$, which is a 25 percent reduction. On the other hand, as seen in the figures, there is also a strengthening of the shock. For the case illustrated, P_2/P_1 grows from 2.94 to 4.27. From Equation 16, a pressure ratio of this magnitude corresponds to a jump in Mach number from 1.60 to 1.90, or a growth in shock speed from $516\,\mathrm{m\,/\,s}$ to $613\,\mathrm{m\,/\,s}$. The shock speed, however, accelerates to only $590\,\mathrm{m\,/\,s}$,

56

Figure 27 Modification of neutral pressure profile for an accelerating shock (solid) due to additional ionization, $\delta = 300$ and $\Delta T_e = 300\,\mathrm{K}$. Control case is dashed. Normalized to upstream pressure. Weakening and broadening of the shock was not observed.

as seen in Figure 26. It falls short of the anticipated 613 m/s possibly because the shock no longer resembles a Riemann shock, meaning that it no longer has the level pressure reservoir. This modification of the neutral shock structure is the result of the transport of neutrals from Region 2 to the shock front due to ion-neutral coupling, as made evident by the shift in neutral density in Figure 28.

Equation 73 predicted the exponential growth of ion density with time. When the shock had reached $x = 0.9\,\mathrm{m}$, the ion density in the vicinity of the shock had increased by four orders of magnitude, as illustrated in Figure 29. From Figure 26, the shock experienced an appreciable acceleration at $t = 0.45\,\mathrm{ms}$, which corresponds to a local fractional ionization at the shock front of approximately 1×10^{-3}, as seen in Figure 30. This is in very good agreement with the threshold fractional ionization, α_{ia}, described in the beginning of the chapter.

It is possible to approximate the shock speed as a function of time. In Figure 30 α_S is shown as a function of time. In Figure 17 the shock speed is shown as function of α_S. If the gas was fully ionized, the fractional ionization would be unity and
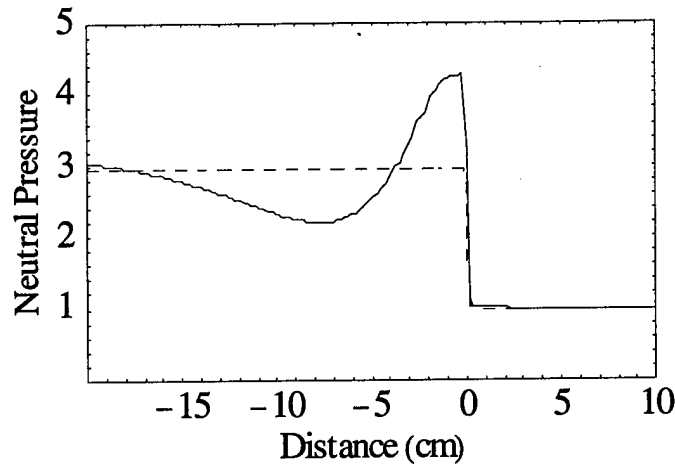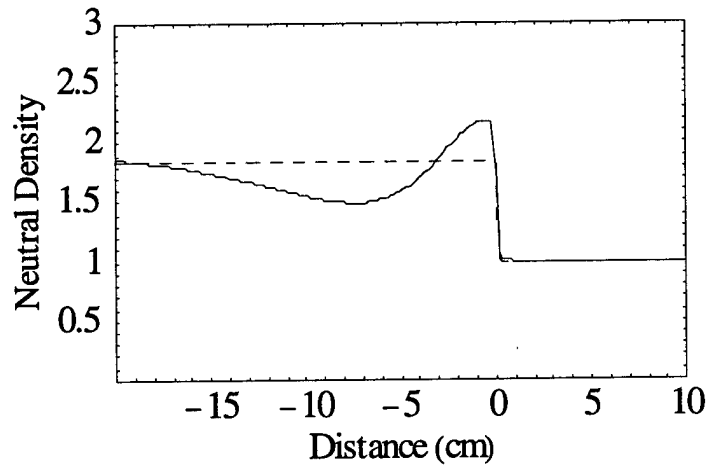
Figure 28   Modification of neutral density profile for an accelerating shock (solid) due to additional ionization, $\delta = 300$ and $\Delta T_e = 300\,\mathrm{K}$. Control case is dashed. Normalized to upstream density. Weakening and broadening of the shock was not observed.
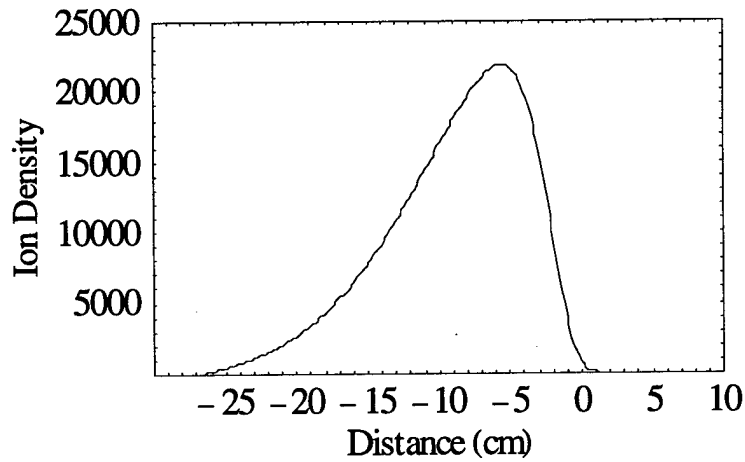
Figure 29   Ion density due to additional ionization at the shock, $\delta = 300$ and $\Delta T_e = 300\,\mathrm{K}$. Density is normalized to upstream ion density. In the vicinity of the shock, the local value of α grows to approximately 2×10^{-2}, which results in a bidirectional pressure gradient in Region 2.
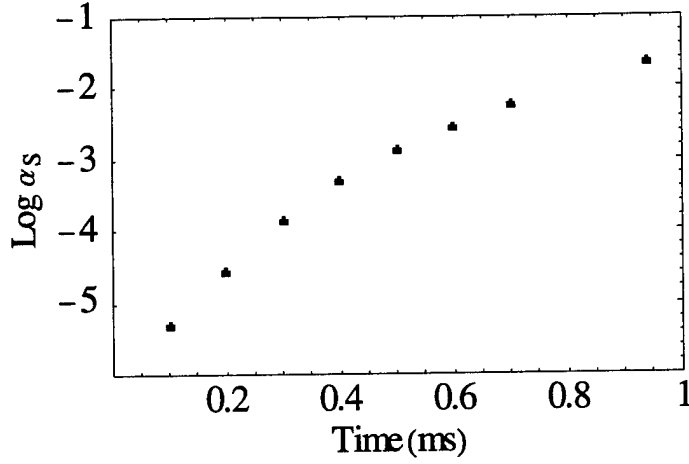
Figure 30   Growth of local fractional ionization at the shock front due to additional ionization.

the shock would propagate at the ambient ion-acoustic velocity, which is $2196\,\text{m}/\text{s}$ according to Equation 23 for test conditions. Incorporating this data point into the data shown in Figure 17, the data can be approximated by the following curve:

$$c = c_0(1 + 3.28\alpha^{0.676}) \tag{76}$$

where c_0 is the shock velocity for the unionized Riemann solution, namely, in this case, $513\,\text{m}/\text{s}$. The data in Figure 30 can be approximated by

$$\alpha_S = 0.02718(\frac{t}{1\,\text{ms}})^{4.323} \tag{77}$$

Combining these two relationships yields

$$c = c_0(1 + 0.287(\frac{t}{1\,\text{ms}})^{2.92}) \tag{78}$$

This curve is plotted along with the shock propagation data in Figure 31. Although the curve follows the general trend of the numerical solution, the curve predicts a much higher velocity than the results of the numerical solution. The disparity could

59
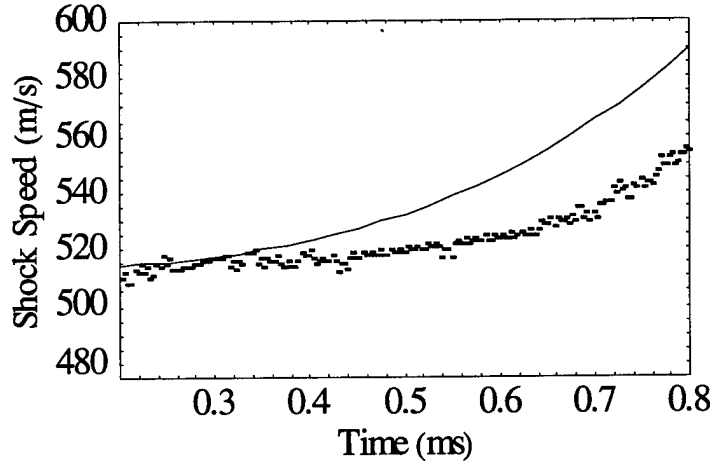
Figure 31   Acceleration of shock due to additional ionization compared to prediction.

be the result of estimating two exponential functions from a limited number of data points, or the result of the assumption that the values of α_S are always exactly at the neutral shock front, which is not always the case as seen in Figure 29.

In spite of the exponential increase in ion density evident in Figure 29, the ion density profile no longer resembles that of a Riemann shock. In addition to the pressure gradient associated with the shock, there is also a negative pressure gradient that causes ions to move against the direction of shock propagation and into Regions 2 and 3. This also results in an extended negative electric field region behind the shock, which extends to the contact discontinuity, as seen in Figure 32. The sharp negative spike in the field may be an artifact of the numerical solution, since it was necessary to inhibited electric field effects in the code behind the contact discontinuity. Even though the concern of the present research is with the field in the vicinity of the shock, the total potential is obtained by integrating over the entire negative and positive field regions, just as in Section 4.1.3. The potential drop delivered by the positive field is approximately $-19\,\text{V}$ and the potential drop of the negative portion is $+11\,\text{V}$; therefore, giving a total potential drop of $-8\,\text{V}$. The evolution of the potential as the shock propagates and the ion density builds
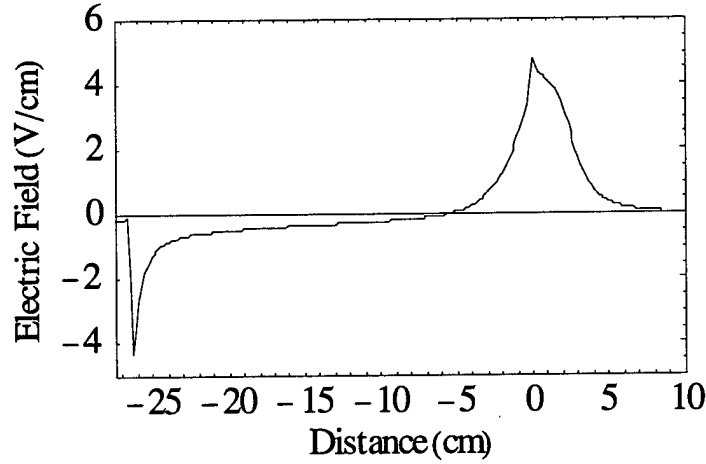
Figure 32   Growth and broadening of electric field due to additional ionization at the shock, $\delta = 300$ and $\Delta T_e = 300\,\mathrm{K}$. Total potential due to this field is approximately -8 V.

is illustrated in Figure 33. Incidentally, shocks generally began to accelerate when they experienced a potential drop of $-6\,\mathrm{V}$. This high potential cannot be the cause of the acceleration as shown above; however, the potential enhances the ion-acoustic waves by way of accelerating the charged particles. The electric field strength was observed to increase with additional ionization over the control case by a factor of 2.5, and the width increased by a factor of 5 (compare to Figure 15).

Recall from Section 1.3 that Saeks and Kunhardt (35) proposed that the equation of state of a weakly ionized gas should include electrostatic pressure terms. The electrostatic pressure is given by

$$P_E = \frac{1}{2}\epsilon_0 E^2 \tag{79}$$

where the permittivity of free space, ϵ_0, equals $8.85 \times 10^{-12}\,\mathrm{C^2/N\,m^2}$. Given the maximum field strength in Figure 32 of approximately $5\,\mathrm{V/cm}$, the maximum electrostatic pressure is about $1.5 \times 10^{-4}\,\mathrm{torr}$. Compared to the upstream ambient neutral thermal pressure of $30\,\mathrm{torr}$, the electrostatic pressure is negligible. Now

61
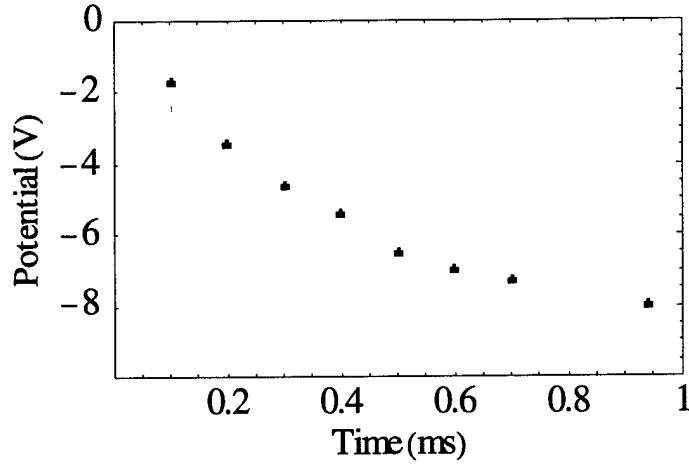
Figure 33   Growth of total potential as a function of time due to additional ioniza-
tion at the shock, $\delta = 300$ and $\Delta T_e = 300\,\mathrm{K}$.

compare the the electrostatic pressure gradient force on the charged component to
the pressure gradient force of the shock. The electrostatic pressure gradient is given
by

$$\frac{dP_E}{d\xi} = \epsilon_0 E \frac{dE}{d\xi} \tag{80}$$

which yields a pressure gradient force per unit mass of

$$F_E = \frac{\epsilon_0 E}{\rho_i} \frac{dE}{d\xi} \tag{81}$$

In the vicinity of the shock, the average field strength is $3\,\mathrm{V\,/\,cm}$, the average field
gradient of $1\,\mathrm{V\,/\,cm^2}$, and the ion mass density is on the order of $10^{-8}\,\mathrm{kg\,/\,cm^3}$. This
yields an average force per mass due to the electric field on the ions is on the order
of $10^{-2}\,\mathrm{N\,/\,kg}$. However, the pressure gradient force per mass due to the shock on
the ions is on the order of $10^5\,\mathrm{N\,/\,kg}$. The pressure gradient force due to the electric
field is insignificant when compared to that of the thermal and dynamic pressure
gradients of the gas as a whole and should not be given any consideration in the
equation of state of weakly ionized gases.
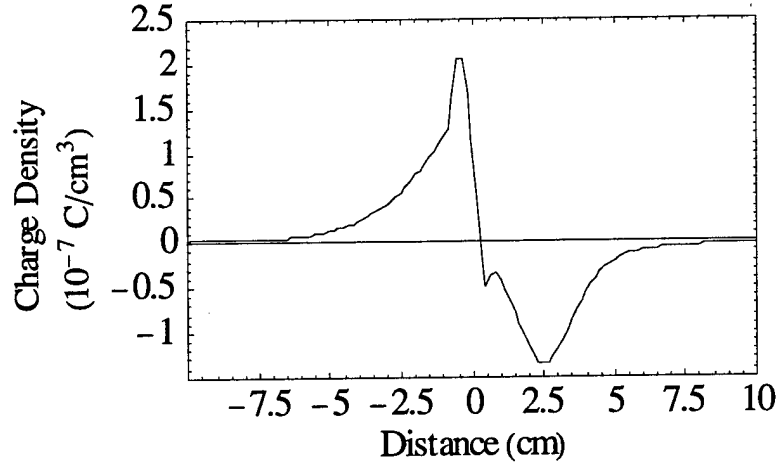
Figure 34   Net charge density. Growth and broadening of electronic double layer due to additional ionization at the shock, $\delta = 300$ and $\Delta T_e = 300\,\mathrm{K}$.

The net charge density in the vicinity of the shock is displayed in Figure 34. Charge neutrality has been maintained to 99.2 percent. The long negative tail of the electric field serves a conduit to draw ions away from the highly concentrated region at the shock front and into the remainder of Region 2, thus expanding the EDL (compare to Figures 12 and 16). This is visible in Figure 35, in which the ion velocity downstream from the shock is reduced to 75 percent of that of the control case.

Significant neutral precursors were observed for cases in which $\Delta T_e \geq 500\,\mathrm{K}$. For the particular case discussed below, $\Delta T_e = 600\,\mathrm{K}$ and $\delta = 100$. The precursor is clearly visible in Figures 36 and 37, with a width of about a centimeter and a maximum pressure of approximately $1.1P_1$. Increased density in the precursor indicates mass transport from Region 2 to Region 1, which must be the result of ion-neutral momentum coupling. These precursors proved to be transient phenomena. The precursor in Figure 36 occurred at $t = 0.43\,\mathrm{ms}$, where it had reached its maximum intensity, well before the shock had reached $x = 0.9\,\mathrm{m}$. By the time the shock had reached $x = 0.9\,\mathrm{m}$, the precursor had diminished below the criteria established at the beginning of this section. In Hilbun's plasma code, neutral pressure,

63
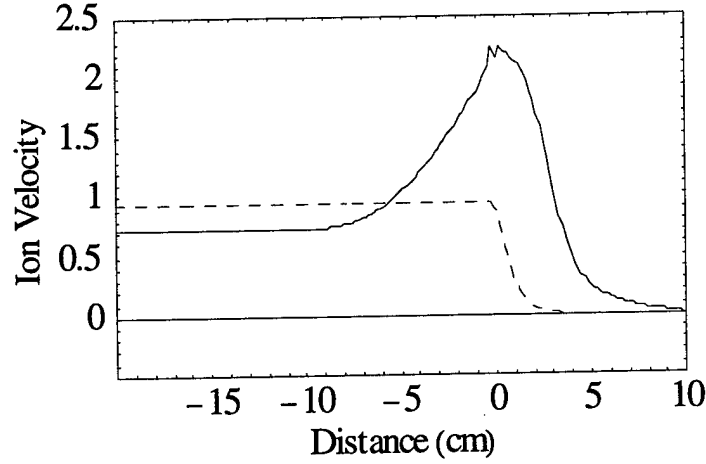
Figure 35   Ion velocity due to additional ionization at the shock, $\delta = 300$ and $\Delta T_e = 300\,\text{K}$. Control case shown for comparison (dashed). Velocities are normalized to upstream ion-neutral thermal velocity, $v = 250\,\text{m}\,/\,\text{s}$. Ions are slowed by the large negative pressure gradient in the region of ionization.

P_n, is normalized by the ambient upstream pressure, P_{n0}, and all calculations use $\hat{P}_n = P_n/P_{n0}$. Shock detection is facilitated by starting from $x = 1\,\text{m}$ and searching down the shock tube until the first pressure rise, $\hat{P}_n \geq \hat{P}_{crit}$, is detected, where $\hat{P}_{crit}$ is arbitrary value just above unity. Precursors were detected by setting $\hat{P}_{crit} = 1.1$.

In conclusion, unrestricted electron impact ionization sustained by a localized increase in electron temperature at the shock front can modify neutral shock structure and propagation. Additional ionization is effective in enhancing ion-acoustic wave damping by raising the local fractional ionization at the shock front to a level conducive to ion-neutral momentum coupling, such that, at the shock, the medium becomes a partially ionized gas, where $\alpha \geq 10^{-3}$. However, research indicates that the shock acceleration in weakly ionized gases does not continue unhampered; therefore, there must be some abating mechanism present.
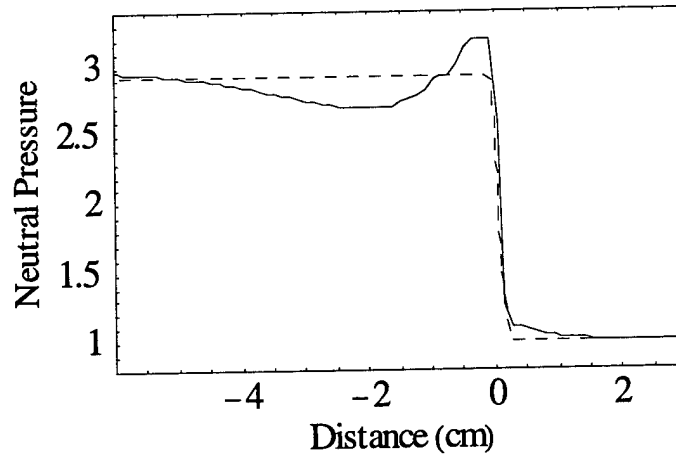
Figure 36   Neutral Precursor.   Neutral pressure profile at the shock front for the parameters $\Delta T_e = 600\,\mathrm{K}$ and $\delta = 100$.   Precursor is clearly visible against the control case (dashed).
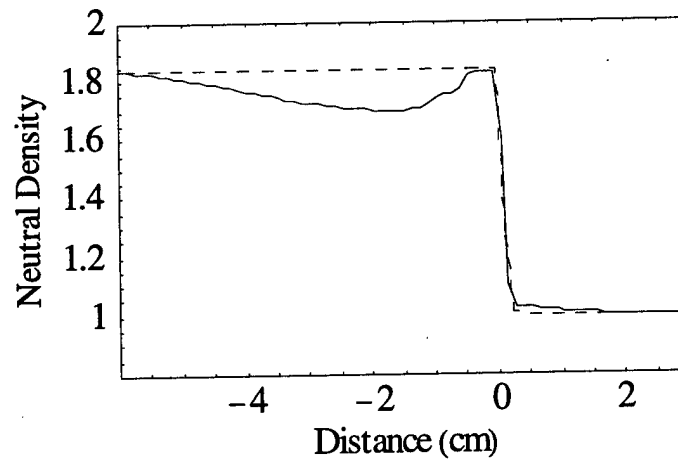
Figure 37   Neutral Precursor.   Neutral density profile at the shock front for the parameters $\Delta T_e = 600\,\mathrm{K}$ and $\delta = 100$.   Precursor is clearly visible against the control case (dashed).   Increased density in the precursor indicates mass transport from Region 2 to Region 1.
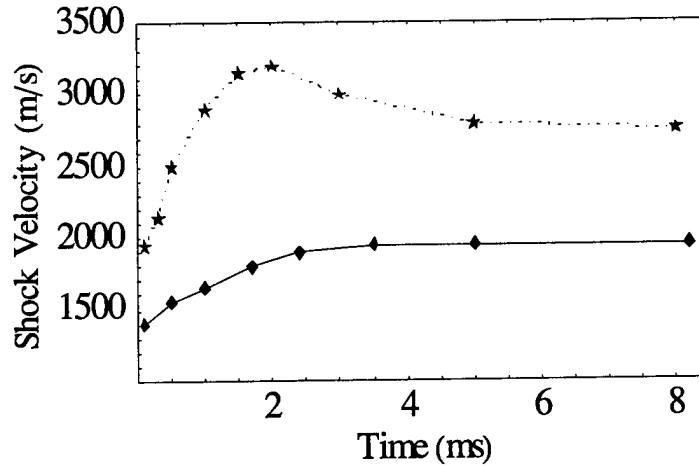
Figure 38   Shock speed as a function of time for a shock in N_2 (dotted) in Ar (solid). Shock enters plasma region at $t = 0$ (Ref: (12)).

4.3 Volumetric Loss of Plasma at the Shock

4.3.1 Development.   Revisiting the shock velocity depicted in Figure 26, all accelerating shocks observed in the current research continued to accelerate until they reached the end of the shock tube. Research, however, indicates that shocks level off in velocity after their initial acceleration ((12), (13), (27)). Figure 38 displays the experimental results obtained by Chutov, et al.,(12) in which the acceleration of the shock leveled off when it entered the a region of weakly ionized argon. For comparison, their results for weakly ionized N_2 are included. Chutov attributes this non-monotonic acceleration in N_2 to vibrational-translational interaction, which is not present in argon. It is apparent then that there is some mechanism at work to mitigate the unabated acceleration of the shock. This section considers volumetric loss of plasma due to ion-electron recombination as a candidate mechanism.

In the absence of applied electric fields and negative ions, the ion-electron recombination equation is given by Raizer (34:60) as

$$Z_{recomb} = (\frac{dn_e}{dt})_{recomb} = -n_i n_e \beta_e \tag{82}$$

66

where β_e is the dissociative recombination coefficient, which is generally on the order of $10^{-7}\,\mathrm{cm}^3/\mathrm{s}$ for diatomic gaseous media. The net rate of ionization events per unit volume per unit time, Z_{net}, is the sum of Equations 68 and 82:

$$Z_{net} = Z_{ion}^e - Z_{recomb} = n_e(k_e n_n - \beta_e n_i) \tag{83}$$

Note that the ion loss term now has an n_i^2 dependence, rather than an n_i dependence as in the unrestricted ionization cases above. In order to restrict net impact ionization to vicinity of the neutral shock front, Z_{net} must be positive in the vicinity of the neutral shock and effectively zero for $\xi \ll 0$ and $\xi \gg 0$, where $n_{i0} = \alpha n_{n0}$. For this condition to be met

$$\beta_{e0} = k_{e0}\frac{n_{n0}}{n_{i0}} = \frac{k_{e0}}{\alpha} = \frac{\sigma_e}{\alpha\sqrt{2\pi}}\sqrt{\frac{k_B T_{e0}}{m_e}}\exp(-\frac{I_P}{k_B T_{e0}}) \tag{84}$$

Raizer states that for the dissociative recombination process of argon ions,

$$Ar_2^+ + e \rightarrow Ar + Ar^*$$
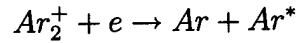
β_e varies as $T_e^{-1/2}$ for temperatures from room temperature to several thousand degrees Kelvin, and varies as $T_e^{-3/2}$ for even higher temperatures. As an approximation, the present research will assume that β_e varies as T_e^{-1}, so that

$$\beta_e(T_e) = \beta_{e0}\frac{T_{e0}}{T_e} = \frac{k_{e0}}{\alpha}\frac{T_{e0}}{T_e} \tag{85}$$

Therefore, where $T_e = T_{e0}$, then $\beta_e = \beta_{e0} = k_{e0}/\alpha$, and the net ionization is zero. Electron impact ionization mitigated by ion-electron recombination was also implemented in Hilbun's plasma code by incorporating Equations 64, 66, 75, and 83, where quasi-neutrality, $n_i \simeq n_e$, is assumed.

67

Figure 39 Ion density profile due to additional ionization mitigated by and recombination at the shock, $\delta = 300$ and $\Delta T_e = 8000\,\mathrm{K}$. Density is normalized to upstream ion density. In the vicinity of the shock, the local value of α grew to approximately 2.7×10^{-5} and remained there.

4.3.2 Results and Analysis. Calculations with input parameters in the range of $\Delta T_e \leq 11,000\,\mathrm{K}$ and $\delta \leq 300$ were in general numerically stable. Dramatic effects on ion and neutral flow variables were not observed, neither were significant accelerations of the shock front. The parameters of the case discussed below are $\Delta T_e = 8000\,\mathrm{K}$ and $\delta = 300$. In Figure 39, the ion density at the shock front increased such that $\alpha_S = 2.5 \times 10^{-5}$, where it remained for the duration of its propagation. This value is greatly diminished from the unrestricted ionization values due to the n_i^2 recombination factor. This value of α_S does not approach the 1×10^{-3} required for effective ion-acoustic wave damping. Consequently, there were no variations in the neutral shock pressure profile. The neutral shock velocity was seen to increase only very slightly, if at all. The general trend in the shock velocity was a change of $2\,\mathrm{m/s}$ over $0.5\,\mathrm{ms}$; however, the uncertainty in the shock velocity calculations was also $\pm 2\,\mathrm{m/s}$. Acceleration of the shock in this case is slight at best.
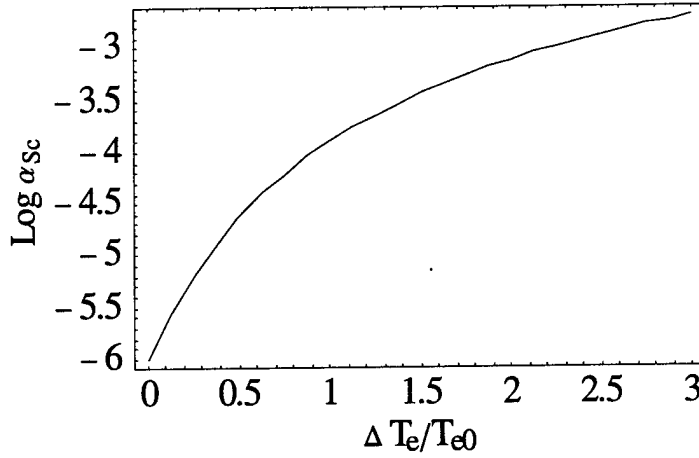
Figure 40   Critical fractional ionization at the shock front as a function of the increase in electron temperature.

The growth of ion density at the shock is limited by the ion-electron recombination. Recall Equation 83:

$$Z_{net} = Z_{ion}^e - Z_{recomb} = n_e(k_e n_n - \beta_e n_i)$$

Ion density grows until $Z_{net} = 0$, at which point $n_i = (k_e/\beta_e)n_n$, if it is assumed that n_n is roughly constant during this process. A cutoff α_S can be determined from Equations 69, 71, and 85:

$$
\begin{aligned}
\alpha_{Sc} &= \frac{k_e}{\beta_e} \\
&= \alpha(1 + \frac{\Delta T_e}{T_{e0}}) \exp(\frac{I_P}{k_B T_{e0}}(1 - (1 + \frac{\Delta T_e}{T_{e0}})^{-1}))
\end{aligned}
\tag{86}
$$

This function is plotted in Figure 40. Clearly, a large increase in electron temperature is required to reach $\alpha_{Sc} = \alpha_{ia}$. These increases in electron temperature, however, caused numerical instabilities.

The electric field, depicted in Figure 41, exhibited the general profile of the variable electron temperature case shown in Figure 23. This is to be expected since

69

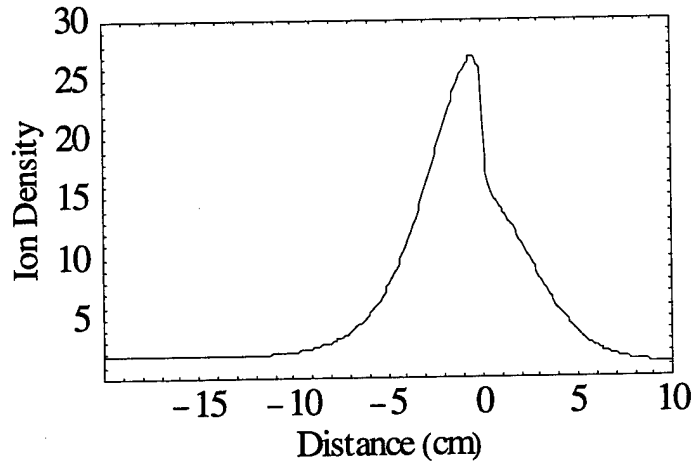Figure 41   Electric field in vicinity of shock due to additional ionization mitigated by recombination at the shock, $\delta = 300$ and $\Delta T_e = 8000\,\mathrm{K}$.

the growth of ion density at the shock is limited, yet the field is still affected by the variation in electron temperature. The field reaches a maximum of approximately $4\,\mathrm{V}\,/\,\mathrm{cm}$ at the shock boundary. It also has a broad positive precursor and negative tail, both features associated with the electron temperature dependence of Equation 67.   The broad positive field region energizes the charged components, but there is insufficient ion density to affect the neutral population.   The broad negative region behind the shock serves as a conduit to draw ions away from the shock front, further reducing the possibility of effective ion-neutral momentum coupling.   Here, the influence is even more profound as seen in Figure 41.   The potential drop of the positive field is $-8\,\mathrm{V}$, and the potential in Region 2 is $+6.5\,\mathrm{V}$.   In spite of the broad extent of the field, the total potential drop delivered by the field is only $-1.5\,\mathrm{V}$.

The net charge density also exhibited some interesting characteristics, as seen in Figure 42. In the absence of the spike in the electric field, the lobes would tend to trap electrons at the shock front. With the spike present, electrons are trapped in a small region just in front of the shock as seen in Figure 42, in contrast to the broad negative charge regions of the previous cases.   The field structure also establishes a *double* EDL, in which there are two regions of net positive charge near the shock

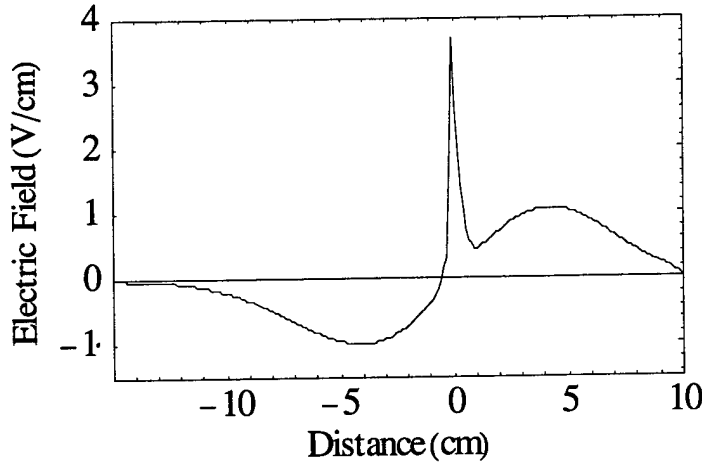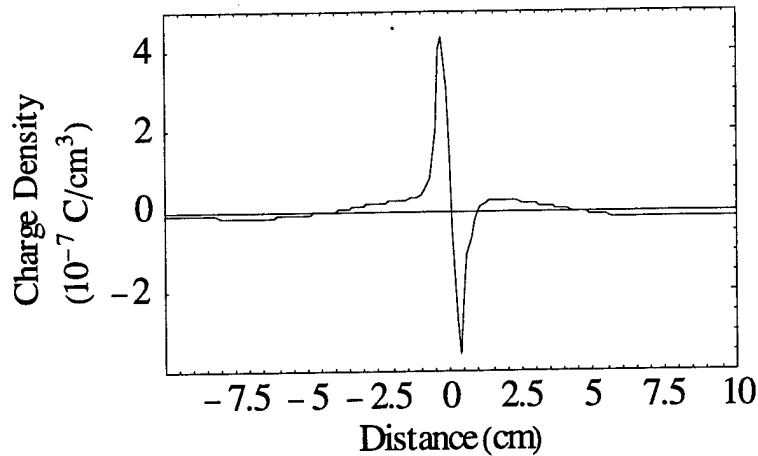Figure 42   Net charge density in vicinity of shock due to additional ionization mitigated by and recombination at the shock, $\delta = 300$ and $\Delta T_e = 8000\,\mathrm{K}$.

front.   In spite of the general negative appearance of the net charge profile, charge neutrality was maintained to within 97.7 percent.

Due to the lack of effects on the neutral shock structure and propagation, it is likely that either ion-electron recombination occurs on a smaller scale than that which occurred in this investigation, or that there are other mechanisms at work in the plasma.   Some of these mechanisms may be hidden in the limitations imposed upon the model, which were discussed in Section 1.3.   These may include energy losses to electronic excitation, diffusion losses, and modifications to electron energy distribution functions.

V. Conclusions and Recommendations

5.1 Conclusions

In Chapter II, several phenomena associated with shock propagation in weakly ionized gases were described. Four of those were investigated in this research:

- Shock waves have an anomalously high propagation velocity.

- The shock front is significantly broadened.

- A precursor exists ahead of the shock wave.

- Shock strength is reduced.

The introduction of a spatially-dependent electron temperature profile greatly affected the charged component for the values of ΔT_e and δ investigated. Three effects on the charged component flow parameters and electric field structure resulted from incorporating this temperature profile. The first was an increase in the charged component precursor width, ξ_0. This was shown to be the result of capturing the local value of T_e, since ξ_0 varies directly with T_e. The second was a general broadening and strengthening of the electric field. This, however, included a negative field region that prevented the total potential drop from growing very large, resulting in a drop of only $-2\,\mathrm{V}$, whereas the potential drop of the unionized Riemann value was $-1.5\,\mathrm{V}$. The third was a variation in the net charge distribution around the shock front as a result of the electric field. All of these effects can be explained by the electric field approximation's dependence on the spatially-dependent electron temperature (Equation 67). There were no discernible effects on the neutral gas, which was expected since the ion density never approaches the level required for efficient ion-neutral momentum coupling.

Although the spatially-dependent electron temperature alone bore little influence on the neutral flow, when coupled with additional electron impact ionization

at the shock front, it yielded striking results. For the range of the parameters ΔT_e and δ investigated, three trends were observed in neutral shock parameters. Steady accelerations of the neutral shocks were observed. There were also modifications of the neutral shock profile. Perhaps the most intriguing result was the appearance of a significant neutral precursor. These results were triggered by an increase in ion density at the shock to the level required for sufficient ion-neutral momentum coupling. It was determined that in order for ion-acoustic wave damping to affect the neutral flow, the local value of α at the shock front must increase to 1×10^{-3}. Given this condition, a time, t_{ia}, and a minimum required ΔT_e were derived for expected accelerations of the shock. Accelerations were observed for values of ΔT_e just greater than the threshold and occurred at times that were half of t_{ia}, as seen in Figure 26.

In Region 2 of the shock tube, the neutral pressure profile deviated significantly from the Riemann solution. A general weakening of the cross-shock pressure ratio, P_2/P_1, was observed. Although, locally at the shock front, there was also an increase in P_2/P_1. This modification of the neutral shock structure is the result of the transport of neutrals from Region 2 to the shock front due to ion-neutral coupling, as made evident by the shift in neutral density in Figure 28.

Significant neutral precursors were observed for higher values of ΔT_e. The precursor is clearly visible in Figure 36, with a width of about a centimeter and a maximum pressure of approximately $1.1P_1$. These precursors proved to be transient phenomena, in which most precursors remained above $\hat{P}_{crit}$ for only 0.03 ms.

The striking modifications to the neutral shock structure and propagation due to unrestricted ionization were mitigated by ion-electron recombination. Due to the n_i^2 recombination factor, the local value of α did not approach the 1×10^{-3} required for effective ion-acoustic wave damping. The electric field exhibited the structure expected from its dependence on the variable electron temperature. The positive portion of the field exhibited two maxima. The smaller maximum is balanced by the

negative portion of the field behind the shock, which serves as a conduit to draw ions away from the shock front, further reducing the possibility of effective ion-acoustic wave damping.

In conclusion, it has been shown that unrestricted electron impact ionization sustained by a localized increase in electron temperature at the shock front can modify neutral shock structure and propagation. Additional ionization is effective in enhancing ion-acoustic wave damping by raising the local fractional ionization at the shock front to a level conducive to ion-neutral momentum coupling, such that, at the shock, the medium becomes a partially ionized gas, where $\alpha \geq 10^{-3}$. However, research indicates that the shock acceleration in weakly ionized gases does not continue unhampered; therefore, there must be some abating mechanism present in weakly ionized gases.

5.2 Recommendations for future study

The present research lifted two of the restrictions imposed upon the previous analytical and numerical treatments. There are many remaining to be conquered. Here they are discussed in order of feasibility. Many of the following physical considerations could feasibly be incorporated into Hilbun's codes. The numerical solutions of the present research essentially rode on the shoulders of Hilbun's work; possible improvements to that work are also outlined below.

Shocks are multi-dimensional phenomena. The problems studied in the present research are limited to one spatial dimension. In his research on the effects of thermal inhomogeneities on shock propagation, Hilbun developed a two-dimensional fluid code (22:28). Plasma effects could be expanded into two dimensions and incorporated into this program.

Although this research effort focused on shock tube problems, much of current research is conducted in glow discharge tubes. In a glow discharge tube, an electric field is applied to the gaseous medium, which causes electronic excitation and ioniza-

74

tion. The ionization is balanced by diffusion losses to the tube walls. The constant baseline electric field of the positive column was not a consideration in the present research, nor were radial losses. After modifying Hilbun's one-dimensional plasma code for two dimensions, glow discharge tube problems could be more accurately modelled.

Any practical investigation of plasma aerodynamics must include diatomic gases. With these species come a host of considerations: the energies associated with rotation, vibration, and dissociation. In his study of post-shock energy addition due to vibrational relaxation, Hilbun developed a one-dimensional, time-dependent, single fluid code (22:103) that takes vibrational energy into account. With great meticulousness, his plasma and vibrational codes could be melded into one. Plasma effects could be introduced into this code. Along these lines, electronic excitation should be considered as well since much energy can be absorbed into excited states, thus reducing the possibility of additional ionization occurring at the shock front.

Several assumptions were made in modelling the electron impact ionization process. One of these assumptions was a steady electron energy distribution function. Another assumption was a constant ionization cross section. As free electrons lose energy to the ionization process, a shift in the electron energy distribution function occurs. Since additional ionization was shown to affect neutral shock structure and propagation characteristics, a purely kinetic approach to the ionization process is warranted.

Charge density gradients, according to the steady-state and time-dependent, two-fluid approximations, vary rapidly just behind the shock. A fixed, laboratory spatial scale may not accurately capture these gradients. A variable spatial scale could be implemented in the vicinity of the shock. For this, the fluid equations must be transformed from the laboratory-fixed frame to the shock-fixed frame. According to Anderson (3:102), the differencing of the FCT algorithm can be reversed to transform to a shock-fixed frame. The real challenge is that shock propagation

in the Riemann problem is nonlinear at the onset of propagation. An algorithm to predict the location of $\xi = 0$ would need to be incorporated as well.

Finally, the two-fluid approximation still stands. This restriction prevents ions and electrons from moving independently of each other, which is necessary in order to fully characterize the double layer influence on shock structure and propagation in weakly ionized gases. The electric field is an approximation based upon the assumption of steady-state electron momentum. In order to fully characterize the electric field and associated charge separation, Poisson's equation must be solved. Appendix B outlines the development of the fluid equations to this end; however, a numerical scheme that can mitigate the restrictive time step is still required.

Appendix A. List of Symbols

The subscripts j and k refer to the neutral, ion, and electron species as appropriate.

a	speed of sound
c	shock speed
c_P	specific heat (constant pressure)
c_V	specific heat (constant volume)
e	elementary charge
E	electric field
f_e	electron velocity distribution
$\overline{F}$	flux vector
I_P	ionization potential
k	ion-acoustic wave number
k_B	Boltzmann's constant
k_e	electron impact ionization coefficient
m	ion-neutral mass
m_e	electron mass
M	Mach number
n_j	species number density
N_{CFL}	Courant-Friedrichs-Levy number
P_j	species pressure
$\widehat{P}_j$	species normalized pressure
$\widehat{P}_{crit}$	normalized shock detection pressure
P_{jk}	inter-species momentum transfer
q	charge
Q	heat addition
Q_{jk}	inter-species energy transfer
s	entropy

$\overline{S_1}$	Euler term source vector
$\overline{S_2}$	species coupling source vector
$\overline{S_3}$	electric field source vector
$\overline{S_4}$	ionization source vector
t	time coordinate
t_{ia}	time to reach ion-acoustic conditions
T_j	temperature
T_P	ionization temperature
u	fluid velocity
$\overline{U}$	vector of conserved variables
V_j	species fluid velocity
$\widehat{V}$	ion/shock velocity ratio
v_{ia}	ion-acoustic velocity
v_j	species thermal velocity
w	thermal energy
x	spatial coordinate
y_j	species shock-fixed velocity
Z_{ion}^e	electron impact ionization rate
Z_{net}	net ionization rate
Z_{recomb}	ion-electron recombination rate
α	fractional ionization
α_{ia}	fractional ionization of ion-acoustic conditions
α_S	local fractional ionization at shock front
β_e	recombination coefficient
γ_j	species ratio of specific heats
δ	electron thermal region width parameter
ΔT_e	electron temperature rise
ϵ_0	permittivity of free space
ζ	net charge density

λ	neutral-neutral mean free path
λ_{jk}	inter species mean free path
μ	Avramenko density parameter
ν_{jk}	inter-species collision frequency
ξ	shock-centered spatial coordinate
$\widehat{\xi}$	shock width parameter
ξ_0	charged precursor width
ρ_j	species mass density
σ_e	electron impact ionization cross section
σ_{jk}	inter-species collision cross section
τ_{jk}	inter-species collision time
v_{ave}	average molecular velocity
v_k	equivalent ionization potential velocity
ϕ	electric potential
ω	ion-acoustic frequency
ω_j	species plasma frequency

Appendix B. Time-dependent three-fluid approximation

The preferred method of analysis of shock propagation in weakly ionized gases is by way of a three fluid approach, in which the continuity, momentum, and energy equations of neutrals, ions, *and* electrons are numerically solved; the development of this method is outlined herein. The present research effort attempted to lift the two-fluid approximation; however, the difference in computational time steps for electrons and heavy particles proved to be prohibitively large to be accomplished within the time and computing limits of this research effort. In the Hilbun's two-fluid solution, ion and neutral velocities were normalized by the ion-neutral thermal velocity (22:202) and the computational time step was on the order of

$$\Delta t_2 \leq N_{CFL} \frac{\Delta x}{v_{ia}} \tag{87}$$

where N_{CFL} is the Courant-Friedrichs-Levy number, which is generally 0.4 and is used to ensure stability (22:219). The three-fluid approach utilized Hilbun's adaptation of the FCT algorithm of Tóth and Odstrcil (38). Therefore, the three-fluid computational time step is of the same form, but incorporates the electron thermal velocity and is on the order of

$$\Delta t_3 \approx \Delta t_2 \sqrt{\frac{m_e}{m}} \approx 10^{-3} \Delta t_2 \tag{88}$$

Therefore, what had once taken an hour to execute would take several weeks. It is possible, however, to reduce the time requirements by a factor of three. Since the motion of the heavy particles varies slowly relative to the electrons, heavy particle variables only need to be updated for every thousand electron computational steps. Unfortunately, this still yields execution times on the order of weeks.

As mentioned above, the three-fluid approach adopts Hilbun's approach of solving the conservation equations for three species.

$$\frac{\partial \overline{U}}{\partial t} + \frac{\partial \overline{F}}{\partial x} = \overline{S}_1 + \overline{S}_2 + \overline{S}_3 + \overline{S}_4 \qquad (89)$$

For three fluids, the vector of conserved variables, $\overline{U}$, becomes

$$\overline{U} = \begin{bmatrix} \rho_n \\ \rho_n V_n \\ \rho_n(\frac{1}{2}V_n^2 + \frac{1}{1-\gamma}\frac{k_B T_n}{m}) \\ \rho_i \\ \rho_i V_i \\ \rho_i(\frac{1}{2}V_i^2 + \frac{1}{1-\gamma}\frac{k_B T_i}{m}) \\ \rho_e \\ \rho_e V_e \\ \rho_e(\frac{1}{2}V_e^2 + \frac{1}{1-\gamma}\frac{k_B T_e}{m_e}) \end{bmatrix} \qquad (90)$$

The flux vector, $\overline{F}$, is given by

$$\overline{F} = \begin{bmatrix} \rho_n V_n \\ \rho_n V_n^2 \\ \rho_n V_n(\frac{1}{2}V_n^2 + \frac{1}{1-\gamma}\frac{k_B T_n}{m}) \\ \rho_i V_i \\ \rho_i V_i^2 \\ \rho_i V_i(\frac{1}{2}V_i^2 + \frac{1}{1-\gamma}\frac{k_B T_i}{m}) \\ \rho_e V_e \\ \rho_e V_e^2 \\ \rho_e V_e(\frac{1}{2}V_e^2 + \frac{1}{1-\gamma}\frac{k_B T_e}{m_e}) \end{bmatrix} \qquad (91)$$

81

The source terms for the Euler equations and species coupling follow those of the two-fluid approximation:

$$
\overline{S}_1 = -\frac{\partial}{\partial x}
\begin{bmatrix}
0 \\
P_n \\
P_n V_n \\
0 \\
P_i \\
P_i V_i \\
0 \\
P_e \\
P_e V_e
\end{bmatrix}
, \quad
\overline{S}_2 =
\begin{bmatrix}
0 \\
P_{ni} + P_{ne} \\
Q_{ni} + Q_{ne} \\
0 \\
-P_{ni} - P_{ei} \\
-Q_{ni} - Q_{ei} \\
0 \\
-P_{ne} + P_{ei} \\
-Q_{ne} + Q_{ei}
\end{bmatrix}
\tag{92}
$$

where P_{jk} represents the momentum gained by species j at the expense of species k, and Q_{jk} represents a similar transfer of energy between the two species. The momentum and energy coupling terms are given by Jaffrin (23:611):

$$
P_{ni} = \frac{4}{3} n_n n_i \sigma_{in} (V_i - V_n) \sqrt{\frac{2m}{\pi} k_B (T_n + T_i)}
\tag{93}
$$

$$
P_{ne} = \frac{8}{3} n_n n_e \sigma_{en} (V_e - V_n) \sqrt{\frac{2m_e k_B T_e}{\pi}}
\tag{94}
$$

$$
P_{ei} = \frac{8}{3} n_i n_e \sigma_{ei} (V_i - V_e) \sqrt{\frac{2m_e k_B T_e}{\pi}}
\tag{95}
$$

$$
Q_{ni} = 2 n_n n_i \sigma_{in} \sqrt{\frac{2}{\pi m} k_B (T_n + T_i)} \{ k_B (T_n - T_i) + \frac{1}{3} m (V_i - V_n)(V_i + V_n) \}
\tag{96}
$$

82

$$Q_{ne} = 8 n_n n_e \sigma_{en} \sqrt{\frac{2 m_e k_B T_e}{\pi}} \{ \frac{k_B}{m} (T_e - T_n) + \frac{1}{3} (V_e - V_n)(V_n + \frac{m_e}{m} V_e) \} \qquad (97)$$

$$Q_{ei} = 8 n_i n_e \sigma_{ei} \sqrt{\frac{2 m_e k_B T_e}{\pi}} \{ \frac{k_B}{m} (T_i - T_e) + \frac{1}{3} (V_i - V_e)(V_i + \frac{m_e}{m} V_e) \} \qquad (98)$$

The electric field source term is given by

$$\overline{S}_3 = E \begin{bmatrix} 0 \\ 0 \\ 0 \\ 0 \\ e n_i \\ e n_i V_i \\ 0 \\ -e n_e \\ -e n_e V_e \end{bmatrix} \qquad (99)$$

where E is the local electric field and e is the elementary charge. Finally, the ionization source term is given by

$$\overline{S}_4 = \begin{bmatrix} -Z_{net} m \\ -Z_{net} m V_n \\ -Z_{net} m (\frac{1}{2} V_n^2 + \frac{1}{1-\gamma} \frac{k_B T_n}{m}) \\ Z_{net} m \\ Z_{net} m V_i \\ Z_{net} m (\frac{1}{2} V_i^2 + \frac{1}{1-\gamma} \frac{k_B T_i}{m}) \\ Z_{net} m_e \\ Z_{net} m_e V_e \\ Z_{net} m_e (\frac{1}{2} V_e^2 + \frac{1}{1-\gamma} \frac{k_B T_e}{m_e}) \end{bmatrix} \qquad (100)$$

In order to prevent the plasma from decaying in the case of the ternary fluid approximation of the Riemann problem, it is either necessary to apply the restriction of $Z_{net} \geq 0$ or apply an ambient electric field to maintain the plasma. Hilbun's two-fluid code is easily expanded to include the electron equations. Nine variables–density, velocity, and temperature for each of the components–are solved using these nine equations. Ideal behavior of the three components is assumed to determine pressures.

The flow variables were non-dimensionalized by the following normalizing parameters: the ambient upstream (Region 1) neutral density, ρ_{n0}, the ambient upstream neutral and electron temperatures, T_{n0} and T_{e0}, respectively, the neutral and electron thermal velocities at their ambient temperatures, v_n and v_e, respectively, and the length of the shock tube, L. Using these parameters, the normalized variables are:

$$x' = \frac{x}{L}, \qquad t' = t\frac{v_e}{L}$$

$$\rho_n' = \frac{\rho_n}{\rho_{n0}}, \qquad \rho_i' = \alpha\frac{\rho_i}{\rho_{n0}}, \qquad \rho_e' = \alpha\frac{m_e}{m}\frac{\rho_e}{\rho_{n0}}$$

$$T_n' = \frac{T_n}{T_{n0}}, \qquad T_i' = \frac{T_i}{T_{n0}}, \qquad T_e' = \frac{T_e}{T_{e0}}$$

$$V_n' = \frac{V_n}{v_n}, \qquad V_i' = \frac{V_i}{v_i}, \qquad V_e' = \frac{V_e}{v_e} \qquad (101)$$

In the three fluid solution, the steady-state electric field approximation (Equation 48) is no longer valid. Therefore, Poisson's equation, Equation 2, must be solved directly at each point in space in order to obtain the field. Recall the one

84

dimensional form of Poisson's equation:

$$\frac{\partial E}{\partial x} = \frac{e(n_i - n_e)}{\epsilon_0}$$

Since the problem is one-dimensional, the net charge density at each point can be treated as an infinite sheet of charge (infinite in the directions normal to the problem's x-direction). With this, the electric field contributions form each point are independent of distance. The field evaluates to

$$E = \frac{e}{\epsilon_0} \{ \int_{-\infty}^{x_0} (n_i - n_e) dx - \int_{x_0}^{\infty} (n_i - n_e) dx \} \tag{102}$$

Bibliography

1. Adamovich, I. V., V. V. Subramaniam, J. W. Rich, and S. O. Macheret. "Phenomenological analysis of shock-wave propagation in weakly ionized plasmas," *AIAA Journal*, 36(5):816-822 (May 1998).

2. Aleksandrov, A. F., et al. "A possible mechanism for interaction of a shock wave with a decaying plasma in air," *Sov. Phys. Tech. Phys.*, 31(4):468-469 (April 1986).

3. Anderson, D. A., J. C. Tannehill, and R. H. Pletcher. *Computational Fluid Mechanics and Heat Transfer.* Hemisphere Publishing Corporation, 1984.

4. Anderson, Jr., John D. *Modern Compressible Flow.* McGraw-Hill, Inc., 1990.

5. Avramenko, R. F., A. A. Rukhadze, and S. F. Teselkin. "Structure of a shock wave in a weakly ionized nonisothermal plasma," *JETP Lett.*, 34(9):463-466 (1981).

6. Basargin, I. V., and G. I. Mishin. "Shock-wave propagation in the plasma of a transverse glow discharge in argon," *Sov. Tech. Phys. Lett.*, 11(2):85-87 (February 1985).

7. Basargin, I. V., and G. I. Mishin. "Precursor of shock wave in glow-discharge plasma," *Sov. Tech. Phys. Lett.*, 15(4):311-312 (April 1989).

8. Bedin, A. P., and G. I. Mishin. "Ballistic studies of the aerodynamic drag on a sphere in ionized air," *Tech. Phys. Lett.*, 21(1):5-7 (January 1995).

9. Bertin, J. J., and M. L. Smith. *Aerodynamics for Engineers, 2nd Edition.* Prentice-Hall, Inc., 1989.

10. Burden, R. L., and J. D. Faires. *Numerical Analysis, 6th Edition.* Brooks/Cole Publishing Company, 1997.

11. Bystrov, S. A., I. S. Zaslonko, Yu. K. Mukoseev, and F. V. Shugaev. "Precursor ahead of a shock front in an RF discharge plasma," *Sov. Phys. Dokl.*, 35(1):39-40 (January 1990).

12. Chutov, Yu. I., V. N. Podol'skii, and D. A. Braion. "Explosive waves in an evolving gas discharge," *Sov. Tech. Phys. Lett.*, 17(2):101-102 (February 1991).

13. Chutov, Yu. I, and V. N. Podol'skii. "Shock waves in gas-discharge plasma," *Journal of Engineering Physics and Thermophysics*, 62(5):504-509 (May 1992).

14. Evtyukhin, N. V., et al. "On the nature of shock wave acceleration in glow discharge plasma," *Sov. J. Chem. Phys.*, 3(9):2080-2089 (1986).

15. Ganguly, B. N. and P. Bletzinger. "Shock Wave Dispersion in Nonequilibrium Plasmas," *AIAA Paper 96-4607* (1996).

16. Ganguly, B. N., P. Bletzinger, and A. Garscadden. "Shock wave damping and dispersion in nonequilibrium low pressure argon plasmas," *Phys. Lett. A*, 230(1997):218-222.

17. Gombosi, Tamas I. *Gaskinetic Theory.* Cambridge University Press, 1994.

18. Gordeev, V. P., A. V. Krasil'nikov, V. I. Lagutin, and V. N. Otmennikov. "Experimental study of the possibility of reducing supersonic drag by employing plasma technology," *Fluid Dynamics*, 31(2):313-317 (1996).

19. Gorshkov, V. A., A. I. Klimov, G. I. Mishin, A. B. Fedotov, and I. P. Yavor. "Behavior of electron density in weakly ionized nonequilibrium plasma with a propagating shock wave," *Sov. Phys. Tech. Phys.*, 32(10):1138-1141 (October 1987).

20. Gridin, A. Yu., A. I. Klimov, and G. I. Mishin. "Structure of a shock wave in the plasma of a non-steady-state glow discharge with ultraviolet radiation," *Sov. Tech. Phys. Lett.*, 16(4):295-297 (April 1990).

21. Gurijanov, E. P., and P. T. Harsha. "AJAX: New Directions in Hypersonic Technology," *AIAA Paper 96-4609* (November 1996).

22. Hilbun, William M. "Shock waves in nonequilibrium gases and plasmas," Doctoral Dissertation, Air Force Institute of Technology, 1997.

23. Jaffrin, Michel Y. "Shock Structure in a Partially Ionized Gas," *The Physics of Fluids*, 8(1):606-625 (1965).

24. Jones, W. D., H. J. Doucet, and J. M. Buzzi. *An Introduction to the Linear Theories and Methods of Electrostatic Waves in Plasmas.* New York: Plenum Press, 1985.

25. Kittel, C., and H. Kroemer. *Thermal Physics, 2nd Edition.* New York: W. H. Freeman and Company, 1997.

26. Klimov, A. I., A. N. Koblov, G. I. Mishin, Yu. L. Serov, and I. P. Yavor. "Shock wave propagation in a glow discharge", *Sov. Tech. Phys. Lett.*, 8(4):192-193 (1982).

27. Klimov, A. I., G. I. Mishin, A. B. Fedotov, and V. A. Shakhotov. "Propagation of shock waves in a non-steady-state glow discharge," *Sov. Tech. Phys. Lett.*, 15(10):800-802 (October 1989).

28. Mishin, G. I. "Shock waves in a weakly ionized nonisothermal plasma," *Sov. Tech. Phys. Lett.*, 11(3):112-114 (1985).

29. Mishin, G. I., Yu. L. Serov, and I. P. Yavor. "Flow around a sphere moving supersonically in a gas-discharge plasma," *Sov. Tech. Phys. Lett.*, 17(6):413-416 (June 1991).

30. Mishin, G. I., A. I. Klimov, and A. Yu. Gridin. "Measurements of the pressure and density in shock waves in a gas discharge plasma," *Sov. Tech. Phys. Lett.*, 17(8):602-604 (August 1991).

31. Mishin, G. I., "Total pressure behind a shock wave in weakly ionized air," *Tech. Phys. Lett.*, 20(11):857-859 (November 1994).

32. Mishin, G. I. "Sonic and shock waves in a gas-discharge plasma," *Appl. Phys. Lett.*, 71(1):49-51 (7 July 1997).

33. Rees, M. H. *Physics and Chemistry of the Upper Atmosphere.* Cambridge: Cambridge University Press, 1989.

34. Raizer, Yu. P. *Gas Discharge Physics.* Springer-Verlag, 1991.

35. Saeks, R., and E. Kunhardt. "Analysis of the electronic double layer effect in weakly ionized gas reduction," Proceedings of the 2nd Weakly Ionized Gases Workshop, Norfolk, VA, 24-25 April 1998, p. 113-117.

36. Sirghi, L., K. Ohe, and G. Popa. "Interactions between ionization waves and potential structure formed at a constriction of the DC He positive column," *J. Phys. D.: Appl. Phys.*, 30(1997):2431-2440.

37. Sturrock, Peter. *Plasma Physics.* Cambridge University Press, 1994.

38. Tóth, G., and D. Odstrčil. "Comparison of some flux corrected transport and total variation diminishing numerical techniques for hydrodynamic and magnetohydrodynamic problems," *Journal of Computational Physics, 128*:82-100 (1996).

39. Vanderlinde, Jack. *Classical Electromagnetic Theory.* John Wiley & Sons, Inc., 1993.

40. Zel'dovich, Ya. B., and Yu. P. Raizer. *Physics of Shock Waves and High-Temperature Hydrodynamic Phenomena, Volume I.* New York: Academic Press, 1966.

Vita

Captain Shannon L. Walker was born at Oak Harbor, WA, on December 2, 1968. He graduated from Norfolk Christian High School in June 1987 and entered Virginia Polytechnic Institute and State University the following September. He graduated in May 1991 with a B.S. in aerospace engineering, and was commissioned as a 2nd Lieutenant in the Unites States Air Force. His first assignment sent him back to school to the Basic Meteorology Program of the Air Force Institute of Technology (AFIT) at Florida State University, Tallahassee, FL. Upon completing his certification in April 1992, he was reassigned to the 355th Operations Support Squadron at Davis-Monthan AFB, AZ, where he served as the wing weather officer. He also served as the joint task force staff weather officer for Operation Southern Watch in Riyadh, Kingdom of Saudi Arabia, during the hot summer of 1993. In the days when officers could volunteer for assignments, Captain Walker secured an engineering position at the 6th Space Operations Squadron at Offutt AFB, NE, in August 1994. By 1996, he was responsible for all on-orbit satellite engineering activities of the Defense Meteorological Satellite Program, and directed post-launch test and checkout operations in April 1997. In August of that year, he entered AFIT to complete his master's degree in space and solar physics. Upon graduation in March 1999, he was reassigned to the 55th Space Weather Squadron at Schriever AFB, CO. Captain Walker is married to the former Deborah Crites of Colonial Heights, VA, and they have one daughter, Karen Marie (3).

Permanent address: 8325 Friden St
Norfolk, VA 23518

REPORT DOCUMENTATION PAGE

Form Approved
OMB No. 0704-0188

1. AGENCY USE ONLY *(Leave blank)*	2. REPORT DATE March 1999	3. REPORT TYPE AND DATES COVERED

4. TITLE AND SUBTITLE
Double Layer Effects on Shock Wave Propagation

5. FUNDING NUMBERS
None

6. AUTHOR(S)
Shannon L. Walker, Capt, USAF

7. PERFORMING ORGANIZATION NAME(S) AND ADDRESS(ES)
AFIT/ENP
2950 P St
Wright-Patterson AFB, OH 45433
Advisor: William F. Bailey, COMM: (937) 255-3636 ext. 4501
Email: william.bailey@afit.af.mil

8. PERFORMING ORGANIZATION REPORT NUMBER

AFIT/GAP/ENP-15

9. SPONSORING/MONITORING AGENCY NAME(S) AND ADDRESS(ES)
AFRL/PR, Air Force Research Laboratory, Propulsion Directorate
Bldg 18
1950 Fifth St.
Wright-Patterson AFB, OH 45433-7251
Dr. Bish Ganguly COMM: (937) 255-2923

10. SPONSORING/MONITORING AGENCY REPORT NUMBER

11. SUPPLEMENTARY NOTES

12a. DISTRIBUTION AVAILABILITY STATEMENT
Approved for public release; distribution unlimited

12b. DISTRIBUTION CODE

13. ABSTRACT *(Maximum 200 words)*

An analysis and assessment of two mechanisms in plasma shock interactions was conducted under conditions typically encountered in a weakly ionized glow discharge. The mechanisms of a spatially-dependent electron temperature and additional electron impact ionization at the shock front were examined for effects on shock structure and propagation. These mechanisms were incorporated into an existing one-dimensional, time-dependent, fluid dynamics code that uses the Riemann problem as a basis and numerically solves the Euler equations for two fluids: the neutral gas and the charged component. The spatial variation in electron temperature was modeled as a shock-centered rise in temperature. Additional ionization was modeled by incorporating a variable electron temperature and a quasi-kinetic collision function, for both unrestricted ionization and ionization mitigated by ion-electron recombination. Introduction of a spatial variation in electron temperature resulted in a broadening and strengthening of the electric field associated with the electronic double layer (EDL) at the shock front. Results of unrestricted ionization were a broadening and strengthening of the electric field associated with the EDL, an acceleration of the neutral shock front, and the development of a neutral precursor ahead of the shock. Ion-electron recombination was seen to reduce these effects.

14. SUBJECT TERMS
Shocks, Electronic Double Layer, Plasma Aerodynamics, Non-equilibrium Ionized Gases

15. NUMBER OF PAGES
101

16. PRICE CODE

17. SECURITY CLASSIFICATION OF REPORT	18. SECURITY CLASSIFICATION OF THIS PAGE	19. SECURITY CLASSIFICATION OF ABSTRACT	20. LIMITATION OF ABSTRACT
Unclassified	Unclassified	Unclassified	UL